

**Full title:** Reliability of Contrast-Based Automated Fracture Detection from Decimeter Resolution Aerial Imagery

**Abbreviated title:** Reliability of Automated Fracture Detection from Aerial Imagery

**Authors:** G. Amicarelli<sup>1\*</sup>, M. T. Ireland<sup>2</sup>, C. T. Davie<sup>1</sup>

**Author Affiliations:** <sup>1</sup>School of Engineering, Newcastle University, Newcastle upon Tyne, UK, <sup>2</sup>School of Natural and Environmental Sciences, Newcastle University, Newcastle upon Tyne, UK

**Correspondence:** [G.amicarelli@newcastle.ac.uk](mailto:G.amicarelli@newcastle.ac.uk)

**ORCID:**

G.A. <https://orcid.org/0009-0002-7219-9517>

M.T.I. <https://orcid.org/0000-0001-9777-0447>

C.T.D. <https://orcid.org/0000-0003-2770-9178>

### **PREPRINT STATEMENT**

This manuscript has not been peer-reviewed, it has been submitted to EarthArXiv as a preprint. A subsequent version of this manuscript may have slight edits and changes present. This manuscript has been submitted for publication in Tektonika. If accepted, the final version of this manuscript will be available via the 'Peer-reviewed Publication DOI' link on the right-hand side of this webpage.

#### 1. Abstract

Aerial imagery that captures outcrop exposures of rocks enables the characterization of structural discontinuities such as faults and fractures across large and difficult-to-access areas. These datasets provide an opportunity to analyze the characteristics of fault and fracture networks as analogues for the subsurface.

The application of automated interpretation methods to imagery has the potential to reduce subjectivity, increase efficiency, and improve reproducibility. While these methods are commonly used with high-resolution images, the widespread availability of decimeter-resolution imagery, means that demonstrating the reliability of automated methods with decimeter resolution data could significantly extend their application. This study investigates the reliability of two automated fracture detection methods using decimeter resolution imagery and specifically the methods' sensitivity to contrast between rock mass and fractures.

The results indicate that: 1) at lower contrast thresholds, the average feature length increases while the number of feature intersections decreases; 2) extracted features demonstrate reduced robustness in discontinuous outcrop exposures. It is crucial to note that these findings presume a scenario where the rock mass exhibits high contrast, and fractures are characterized by low contrast. The findings demonstrate that automated feature detection is reproducible but currently produces very unreliable results. The use of these methods requires a detailed understanding of how image properties and the parameters defined in detection method impact the resultant features detected. The use of automated methods with decimeter resolution imagery requires a clearly defined criteria to quality check the results.

## 2. Introduction

Faults and fracture networks in rock masses influence both the storage and flow of fluids and serve as important indicators of stress and strain histories (Gudmundsson 2011). These networks can both facilitate and hinder fluid flow (Miranda et al. 2020) and reliably characterizing these networks is crucial in hydrogeology and geoenergy, especially for rocks with low matrix permeability (Berkowitz 2002). This includes applications such as geological disposal of radioactive

waste and identifying pathways for contaminants (Bear 1993; Witherspoon, Cook, and Gale 1980), as well as geothermal energy where fracture networks act as permeability pathways for brines (Pruess and Narasimhan 1982; Singhal and Gupta 2010).

Outcrops provide invaluable analogues for in-situ rocks at depth enabling detailed characterization of fault and fracture networks (e.g., Howell, Martinius, and Good 2014). By studying exposed rock formations, geologists gather critical geometric data often limited in subsurface studies, improving the accuracy of geological models (Bertrand, Géraud, and Diraison 2021). These analogues offer insights into the spatial relationships and connectivity of fractures, supplementing sparse subsurface data from wells and seismic surveys, and are essential for understanding reservoirs and predicting fluid flow (Newell and Shariatipour, 2016). Images of outcrops provide therefore a unique dataset from which to interpret fault and fracture networks (e.g., Castaing et al. 1996; Gabrielsen and Braathen 2014; Tartaglia et al. 2022). Image analysis describes various techniques and processes aimed at extracting meaningful information from images (e.g., Voorn et al., 2013; Weismüller et al., 2020). It plays a critical role in fields like geology, where it is used to distinguish and characterize features such as faults and fractures. The recent advances in remote sensing acquisition technologies such as drones have profoundly transformed the ability to capture and use imagery, enabling the characterization of structural features across large areas of exposure and in traditionally inaccessible locations (Saibi et al. 2018). However, the proliferation of such data has made manual extraction of geological information increasingly impractical (Thiele et al. 2017) and the use of automated interpretations offer improved efficiencies (Chen et al. 2021; Prabhakaran et al. 2019) and can mitigate the subjective bias of manual interpretations (Andrews et al. 2019; Bond et al. 2007; Wilson, Bond, and Shipley

2019). An early example of image processing for feature detection is the Canny edge detection method (Canny 1986), and this was followed by advancements in edge detection algorithms and the integration of rudimentary machine learning techniques (Cracknell and Reading 2014; Harvey and Fotopoulos 2016; Kozlovska et al. 2023). The use of automated techniques for extracting features from imagery has been applied to satellite imagery (e.g., Hung, Batelaan, and Smedt 2005; Sarp 2005) and increasingly drone imagery (Prabhakaran et al. 2019; Weismüller et al. 2020). Lower resolution imagery (~25 cm), referred to as 'decimeter-resolution imagery,' is more readily available (Santos and Rapp 2019; Taylor and Lovell 2012). The availability and accessibility of open license aerial imagery varies worldwide, averaging 0.3m for selected metropolitan areas, 0.5m across the US and Europe, and 0.6-1.2m elsewhere (Esri 2023b). While decimeter resolution imagery has limitations for cm-scale detail, its availability and accessibility make it valuable for mapping meter-scale features, which is useful for applications such as mapping regional geological structural trends and reconnaissance work (Njue 2010; Ray 1960). Although automated detection methods have proven effective with high-resolution imagery (e.g., Prabhakaran et al., 2019, 2021; Weismüller et al., 2020), their effectiveness with decimeter-resolution imagery has received minimal attention.

This work investigates the reliability and reproducibility of automated feature extraction from decimeter-resolution aerial imagery. It evaluates the use of two existing contrast-based automated feature detection methods with decimeter-resolution imagery.

### 3. Methodology & Data

Throughout the study, four different outcrop exposures covered by aerial imagery with comparable resolutions were used to investigate the reproducibility and reliability of automated detection methods (Figure 1A, B, C and D). Fracture networks

were extracted using two different automated methods. Image properties at each locality were quantified using Photoshop and QGIS. Multiple iterations of fracture networks were extracted to investigate the impact of varying key parameters. Similarly to other studies examining fault and fracture network characteristics (e.g., Alexandersen & Andreasen, 2020; Alvarez et al., 2021; Sanderson & Nixon, 2018), properties including fracture length, orientation, and network topology were quantified.

In this study, two fracture detection methods were used: 1) the shearlet-based method developed by Prabhakaran et al. (2019), which detects contrast differences between the rock mass and fractures, and 2) a binary method implemented in ImageJ (Rueden et al. 2017) that also differentiates fractures based on contrast. In both cases, a single raster image with dimensions of 1000px-by-1000px was used as the input. The workflow adopted for both methods and used throughout this investigation is summarized in Figure 2.

The shearlet method by Prabhakaran et al. (2019) is implemented in MATLAB and uses the complex shearlet ridge and edge measure (CoShREM) method described by Reisenhofer et al. (2016), incorporating Otsu thresholding (Otsu, 1979). This method was demonstrated using high-resolution drone imagery. The binary method in ImageJ uses a threshold value to differentiate between foreground and background pixels, considering pixels with intensity greater than the threshold as foreground and those with less intensity as background. Fractures extracted in both methods are represented as lines, a common representation of geological features like faults and fractures in images and maps (Soller, Lindquist, and Matti 2002). Both methods employ a skeletonization process to convert raster representation of features into 1-pixel-wide lines (Rakesh and Rajpreet 2008).

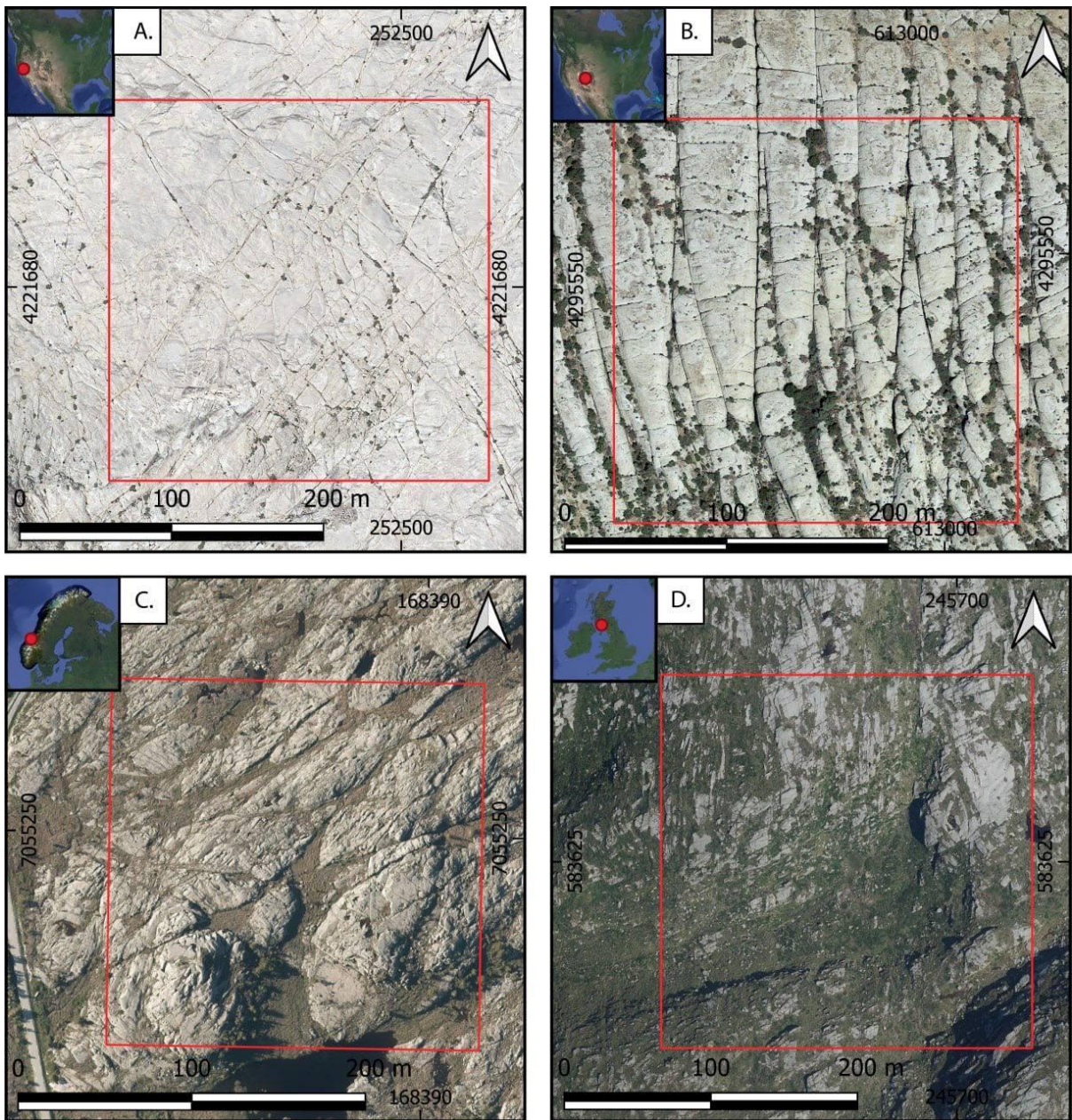


Figure 1: Full-color images of the four study areas: A. Gillet Mountain, Yosemite, USA; B. Salt Valley, Utah, USA; C. Havmyran, Hitra, Norway; D. Craignaw, Galloway, Scotland. The red box in each image indicates the areas used for automated extractions.

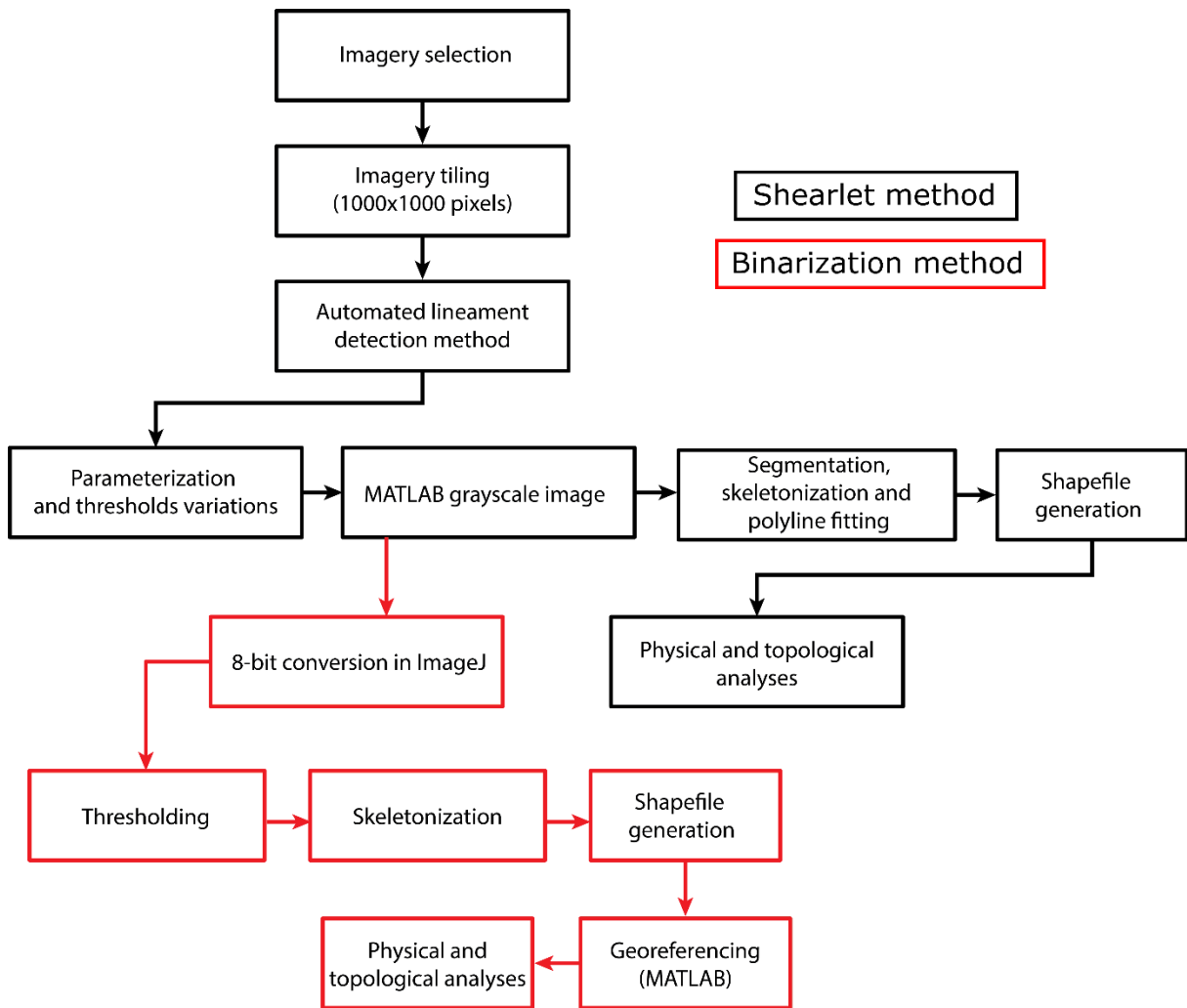


Figure 2: Workflow (Simplified) followed throughout the study. Shearlet Method in black, Binarization Method in red.

### 3.1. Data and Setting

Images of outcrop exposures from four locations are used in this study (Figure 1): 1) Gillet Mountain, Yosemite, USA (Tile A); 2) Salt Valley, Utah, USA (Tile B); 3) Havmyran, Hitra, Norway (Tile C) and 4) Craignaw, Galloway, Scotland (Tile D). Full-band color imagery for each location is shown in Figure 3, with image properties provided in Table 1. See Data Availability for original imagery sources.

Gillet Mountain, Yosemite, constitutes part of the Sierra Nevada Batholith, featuring a rock composition ranging from quartz diorite to granite, emplaced during

the Mesozoic (Bateman and Eaton 1967). The exposure in Salt Valley, Utah, belongs to the Curtis Formation, a component of the Upper Jurassic San Rafael Group (Gilluly and Reeside Jr. 1928). Havmyran, Hitra, is associated with the Smøla-Hitra Batholith, with pluton emplacement occurring from the Mid Ordovician to early Silurian (Bøe et al. 2005), exhibiting composition variations from granitic to granodiorite/tonalite (Gautneb and Roberts 1989). Craginaw, Galloway, pertains to the Loch Doon pluton, emplaced during the Devonian (late Caledonian) (Tindle and Pearce 1981), showcasing a composition ranging from granitic to granodioritic (Gardiner and Reynolds 1932; Hines et al. 2018).

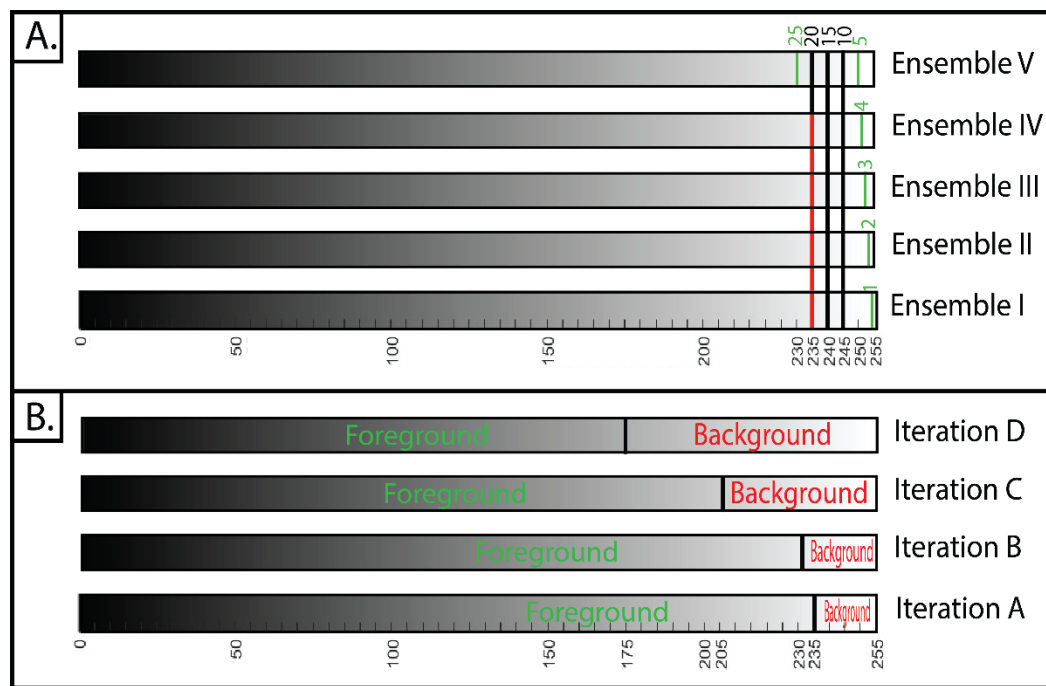


Figure 3: Threshold values for Shearlet (A) and binarization (B) methods. (A) Contrast thresholds used in each ensemble for the Shearlet method, with green lines and numbers indicating threshold values. (B) Foreground/background thresholds applied for the binarization in ImageJ, showing the grayscale spectrum range (foreground) used for lineament extraction.

<b>Location</b>	<b>IR [Cm/pp]</b>	<b>Type of acquisition</b>	<b>Original image</b>	<b>Adjusted</b>	<b>Size (px)</b>	<b>Area (km<sup>2</sup>)</b>	<b>Dominant rock type</b>	<b>Exposed rock %</b>	<b>Average image contrast</b>	<b>Average rock mass contrast</b>	<b>Average vegetation contrast</b>
<b>Yosemite</b>	25	Aerial Survey	RBG	Grayscale	1000x1000	0.063	Granite	98.3	209	209	105
<b>Utah</b>	25	Aerial Survey	RBG	Grayscale	1000x1000	0.07	Sandstone	73.8	162	193	72
<b>Hitra</b>	21	Aerial Survey	RBG	Grayscale	1000x1000	0.045	Granite	51.6	133	175	107
<b>Craignaw</b>	25	Aerial Survey	RBG	Grayscale	1000x1000	0.064	Granite	15.6	99	163	81

*Table 1: Image properties for each locality used in the study.*

## 3.2. Workflow

### 3.2.1. Image Preprocessing

All images, which were originally three-band color images (RGB), were converted to grayscale, with pixel values ranging from 0 (black) to 255 (white), using the `im2gray` function in MATLAB (MathWorks 2023b), which performs a weighted sum of the RGB values from each band. Grayscale images were then cropped into 1000x1000 pixel tiles using Adobe Photoshop (v. 24.3.0). The file format used as inputs for the analysis were tagged image file format (.tif).

### 3.2.2. Image Analysis

To investigate the influence of image properties and outcrop characteristics on extracted feature networks, the following aspects were quantified: 1) percentage of vegetation cover, 2) continuity of the exposed rock area, representing the degree to which exposure of rock can be traced continuously over an area without being interrupted by vegetation, 3) Percentage of foreground pixels, calculated based on the number of pixels above the thresholds defined in Table 2. As threshold values change, so does the amount of detected foreground, and 4) pixel connectedness. The percentage of vegetation cover was quantified using ArcMap 10.8.2's Image Classification Tool. Ten training polygons were traced over vegetated areas to guide the classification algorithm in identifying and extracting vegetated pixels across the image. To quantify the foreground percentage in binary images produced by both approaches, the 'Raster Layer Unique Values Report' function in QGIS was used to compute the count of unique pixel values within the image and then calculate the proportion of foreground to background pixels for both the binarized and skeletonized images. Pixel connectedness in binary and skeletonized images produced using both approaches was determined using MATLAB's Depth-First Search

(DFS) function, which calculates the number of connected regions in a two-dimensional matrix (MathWorks, 2023a).

### 3.2.3. Automated Feature Extraction - Shearlet Method

The Shearlet method, based on the complex shearlet transform method developed by Prabhakaran et al. (2019), is designed to interpret fractures in rock exposures by detecting linear features, or 'ridges,' in an image. Each image is transformed into a ridge probability map representing an ensemble of possible features, with five iterations per ensemble (see Table 1). The resulting ensemble is converted into a skeletonized image, thinning detected ridges into single-pixel clusters (Prabhakaran et al. 2019). Polylines are then fitted through the skeleton image and converted into a georeferenced shapefile for quantifying and characterizing the fracture network.

To assess the impact of varying contrast thresholds, the minimum contrast threshold was varied for each ensemble (see Table 1), while other parameters remained unchanged. The minimum contrast can be any value between 0 to 255.

In all the images used in this study, faults and fractures are most likely represented by low contrast values (<235, see Figure 3A), with the unfractured rock mass mostly represented by higher contrast values. The contrast thresholds used in this method are listed in Table 2. Contrast thresholds used for Ensemble I to IV are shown in Figure 3A. The upper threshold was kept constant at 235 for the first four Ensembles. In Ensemble V, the upper threshold was set at 230, while the lower threshold was set at 250.

<b>Parameters</b>	<b>Values</b>	
<b>Wavelet effective support</b>	5, 8, 10, 12, 15	Base-case Parameters
<b>Scales per octave</b>	1, 2, 3, 4	
<b>Alpha</b>	0, 0.25, 0.5, 0.75, 1	
<b>Offset</b>	0.001, 0.01, 0.1, 1, 2	
<b>Octaves</b>	3.5	
<b>Minimum Contrast</b>		Modified Parameters
<b>Ensemble I</b>	254, 250, 245, 240, 235	
<b>Ensemble II</b>	253, 250, 245, 240, 235	
<b>Ensemble III</b>	252, 250, 245, 240, 235	
<b>Ensemble IV</b>	251, 250, 245, 240, 235	
<b>Ensemble V</b>	250, 245, 240, 235, 230	

*Table 2: Parameters used in the different ensembles of shearlet method for extracting features.*

#### 3.2.4. Automated Extraction - Binarization Method

To evaluate the reliability of the Shearlet method the results were compared to a binarization method implemented using ImageJ (v. 1.53t). Only the image from Yosemite was used for this comparison; the same grayscale image used in the shearlet method was used for consistency. The method separates pixels above and below a defined threshold value (see Figure 3B) to distinguish between foreground and background (ImageJ 2023). For example, a contrast threshold of 175 means that pixels with an intensity value lower than 175 are identified as part of the foreground and pixels with intensity values greater than 175 are designated as background. Four different contrast thresholds were evaluated, which are shown in Table 3.

In each resulting binary image, pixels have a value of either zero (black), which represents foreground, or one (white), which represents background. Skeletonization of the binarized image then fitted lines along the foreground features (ImageJ, 2024). In ImageJ the binarization method does not preserve topology of the networks automatically extracted, meaning that, despite lines being effectively snapped, they

do not form nodes where they intersect. To address this all features within a proximity of 0.000001m (or 1 nanometer) were connected.

<b>Iteration #</b>	<b>Contrast Threshold</b>
<b>A</b>	210
<b>B</b>	205
<b>C</b>	195
<b>D</b>	175

*Table 3: Parameters used for extracting networks automatically using the binarization method in ImageJ*

### 3.2.5. Fracture Network Analysis

To characterize the automatically extracted networks, the following properties were determined for each iteration: 1) number of features, 2) length of each feature, 3) orientation of each feature, 4) density and intensity of the network, and 5) network topology. This analysis was conducted in QGIS using the NetworkGT plugin (Nyberg, Nixon, and Sanderson 2018), which provides functionality for characterizing fault and fracture networks (Nyberg et al. 2018). Length and orientation were calculated using the field calculator in QGIS. Throughout the study, Root Mean Square Error (RMSE) was used to measure the reliability of automated methods. RMSE calculates the standard deviation of the residuals (differences) among the sets of automatically extracted values, indicating how much variability exists across different ensembles and iterations. It provides a quantitative measure of the difference between automated methods. In this study, we do not use a manual interpretation as the reference. Instead, the outputs from each iteration are compared directly with one another. RMSE values between the iterations therefore quantifies how the key fracture property of length differs across these automated outputs, again, with each output effectively serving as a baseline in turn. Consequently, lower residuals

between RMSE indicate that an automated method produce more reliable results. In our analysis, the fracture length from each ensemble were represented using step histograms, and the counts were normalized to a common scale for reliable comparisons. The differences between the normalized histograms were quantified by calculating the root mean square error (RMSE) for each pair of ensembles.

## 4. Results and Observations

### 4.1. Characteristics of Extracted Networks – Shearlet Method

The results of the Shearlet Method for each area of interest are summarized in Figure 4. While most features were traced (Figure 4A, C), others were missed by the method, highlighted in Figure 4B. Additionally, there is a significant proportion of unreliable interpretations, such as features inaccurately traced in shadows and vegetation, particularly evident in Figure 4E, F, G, and H. Figure 5C, F, I, L show the effect of thresholding on fracture length in all four case study areas. Fractures appear more broken down with lower thresholds, indicating that the extraction is more sensitive and results in more connections (Figure 5C). In Ensemble V (Figure 5C, red lines, Ensemble V), the exact same feature is interpreted as continuous, demonstrating how varying thresholds can significantly alter the interpretation of geological features. This highlights the importance of selecting appropriate thresholds to ensure accurate and consistent feature extraction in automated geological analysis.

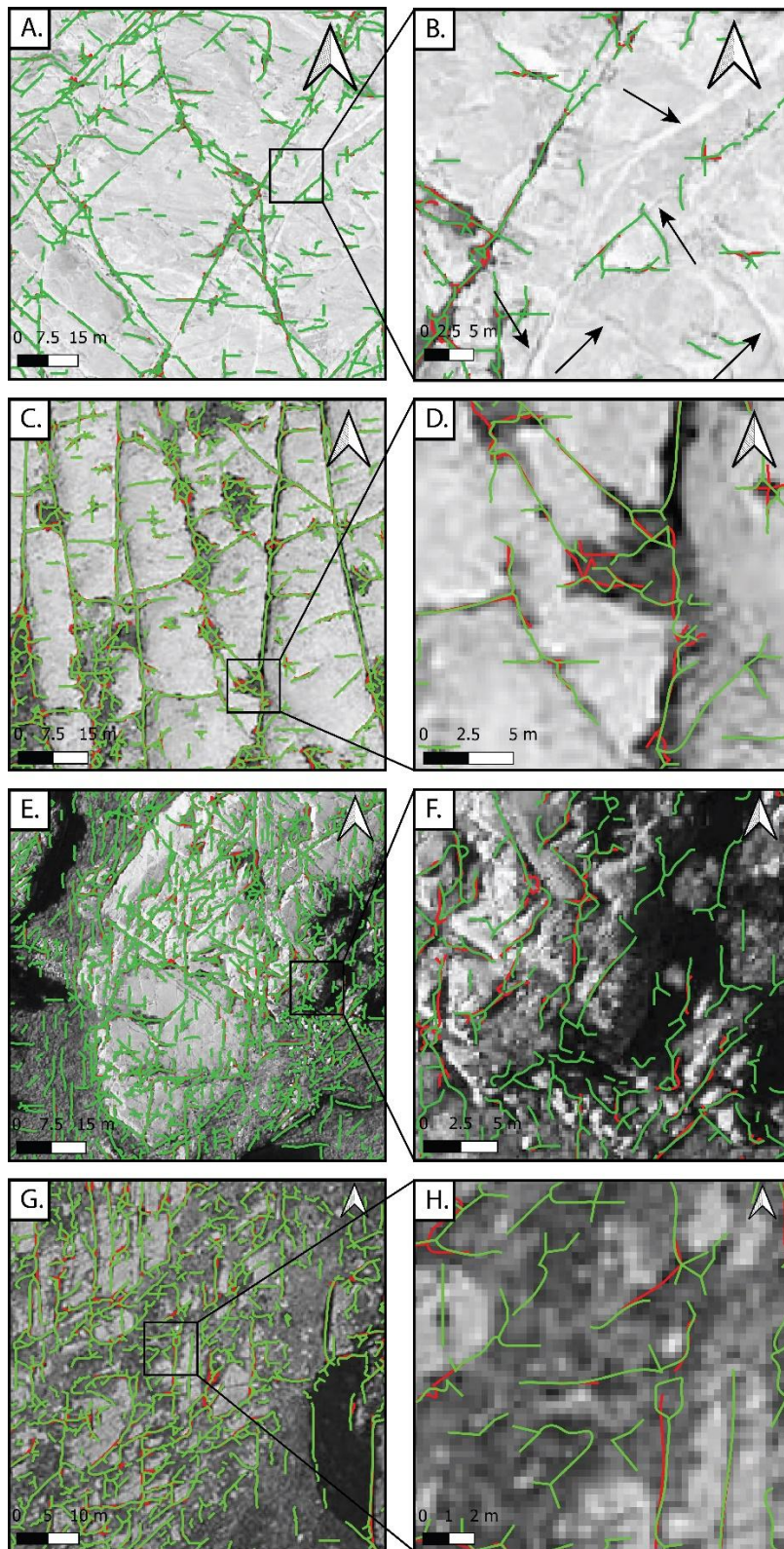


Figure 4: Automated interpretations using the Shearlet Method across different case studies, with Ensemble 1 in green and Ensemble 5 in red. In Yosemite (A and B), high rock

*mass contrast highlights fractures, though Ensemble 1 misses some features, including high-intensity ones (pointed by black arrows). In Utah (C and D), lower contrast reveals wider fractures, but vegetation causes some interference. In Hitra (E and F), extensive vegetation leads to non-geological interpretations. Similarly, in Craignaw (G and H), vegetation and shadows compromise the reliability of lineament tracing.*

#### 4.1.1. Yosemite – Effect of Multi-Contrast Thresholds on Fracture Networks

Ensemble I identified 6,471 features with an average length of 2.17 m, a feature density of 0.103, and 2D intensity of 0.217. In Ensemble II, the number of features decreased by 11.3% to 5,738, with an average length of 2.21 m. The density and 2D intensity decreased to 0.091 and 0.202, respectively. Ensemble III saw a further 8.6% reduction to 5,244 features, with average length increasing to 2.23 m, and density and 2D intensity decreasing to 0.083 and 0.185. Ensemble IV reduced the number of features by 7.97% to 4,836, with an average length of 2.25 m, and density and 2D intensity down to 0.077 and 0.172. In Ensemble V, features sharply decreased by 50.37% to 2,395, with average length increasing to 2.49 m, and density and 2D intensity dropping to 0.038 and 0.095. Topology analysis showed a reduction in nodes from 6,421 in Ensemble I to 2,702 in Ensemble V (Table 4).

In Ensemble I, 4.4% of features had contrast above average rock mass contrast, 91.7% between rock mass and vegetation contrast, and 3.9% below vegetation contrast (Figure 6A). In Ensemble V, 1% were above rock mass contrast, 88.3% between rock mass and vegetation contrast, and 10.8% below (Figure 6B). Major trends (NS and EW) persisted across all ensembles (Figure 7A, B). In Ensemble I, the average feature contrast was 170, which decreased to 169 in Ensemble II. This trend of decreasing contrast continues with Ensembles III and IV, where the average feature contrast was 167 and 165, respectively. By Ensemble V, the average feature contrast significantly dropped to 149 (Table 4). Where the contrast threshold is lower there

are fewer features identified. Interestingly, as shown in Figure 8A, length distribution varies very little, between the Ensembles. While tracing fewer features results in fewer nodes, lower density, and lower intensity, the increase in feature length can be explained by two factors. Firstly, there is a systematic decrease in the number of short features traced using high-intensity pixels (closer to 250) as the contrast threshold decreases (e.g. from Ensemble I to Ensemble V). The presence of high-intensity pixels tend to break up fractures more frequently as they are interpreted as separate features (Figure 5A). This also contributes to an increase in nodes from ensemble to ensemble, as longer features are interrupted by numerous shorter features, creating more connections and intersections within the fracture network. Secondly, as contrast thresholds are reduced, the median length of the network increases. This is attributed to the fact that lower contrast thresholds result in fewer breaks caused by high-intensity pixels, which are otherwise interpreted as separate features. Moreover, the relatively low variability of RMSE observed between ensembles (3.56, Table 4) suggests minimal differences in the length distributions across the five ensembles (Figure 7D, 8A, 9).

#### 4.1.2. Utah – Effect of Multi-Contrast Thresholds Variation on Fracture Network

For Utah, Ensemble I identified 10,751 features with an average length of 1.83 m, density of 0.173, and 2D intensity of 0.281. In Ensemble II the number of features was reduced by 6.2% to 10,085, with an average length of 1.86 m, density of 0.162, and 2D intensity of 0.268. In Ensemble III there was a further reduction to 9,366 features, an average length of 1.89 m, and density and 2D intensity of 0.151 and 0.254. Ensemble IV identified 8,912 features, with an average length of 1.91 m, and density and 2D intensity of 0.143 and 0.243. Ensemble V saw a significant drop to 4,440 features, with an average length of 2.24 m, and density and 2D intensity

decreasing to 0.071 and 0.153. Topology analysis showed a reduction in nodes from 9,401 in Ensemble I to 4,733 in Ensemble V (Table 4).

In Ensemble I, 1.7% of features were above average rock mass contrast, 66.6% between rock mass and vegetation contrast, and 31.7% below vegetation contrast (Figure 6C). Ensemble V had <1% above rock mass contrast, 62.1% between rock mass and vegetation contrast, and 37.6% below (Figure 6D). The dominant trends (NS and EW) persisted across all ensembles (Figure 7C, D).

The average feature contrast decreased from 100 in Ensemble I to 89 in Ensemble V (Table 4). Length variation is more pronounced for the Utah case study, as shown in Figure 8B. Average feature contrast goes down as contrast thresholds are lowered, which is an expected behavior since at lower thresholds the software becomes less sensitive to high intensity pixels. Interestingly, the length distributions between the ensembles start to spread out (Figure 8B), with RMSE between ensembles becoming larger. The calculated average RMSE of 5.20 (Table 4) is higher than the one for Yosemite (3.56) (Figure 9), which corroborates the theory that as the percentage of continuity decreases, the reproducibility of the automated extraction also decreases, resulting in more varied lengths. Overall, there is still a good degree of similarity between the Ensembles for Utah, meaning that the method is still tracing features reliably and maintains a consistent length across ensembles.

#### 4.1.3. Hitra – Effect of Multi-Contrast Thresholds on Fracture Networks

In Hitra, Ensemble I detected 14,652 features averaging 1.47 m in length, with a density of 0.326 and 2D intensity of 0.478. Ensemble II reduced features to 13,440, with an average length of 1.50 m, and density and 2D intensity of 0.299 and 0.447. Ensemble III identified 12,353 features, with an average length of 1.54 m, and density and 2D intensity of 0.275 and 0.422. Ensemble IV reduced features to 11,471, with an average length of 1.57 m, and density and 2D intensity of 0.255 and 0.400. Ensemble

V saw a significant drop to 5,621 features, with an average length of 1.98 m, and density and 2D intensity of 0.125 and 0.232. Topology analysis showed a reduction in nodes from 12,836 in Ensemble I to 5,739 in Ensemble V (Table 4

In Ensemble I, 1.7% of features were above average rock mass contrast, 45.5% between rock mass and vegetation contrast, and 52.8% below vegetation contrast (Figure 6E). In Ensemble V, 1% were above rock mass contrast, 42% between rock mass and vegetation contrast, and 57% below Figure 6F). The dominant trends (NS and NE/SW) persisted across all ensembles (Figure 7E, F).

The average feature contrast decreased from 107 in Ensemble I to 103 in Ensemble V (Table 4: Properties of networks extracted automatically with the shearlet method). This higher vegetation percentage introduces more noise and less distinct geological features into the dataset. As visible Figure 8C, the spread between trendlines starts to be considerable, and again this aligns with our expectations. Rock mass continuity across the Hitra case study is much lower compared to the previous two cases, with a continuity of 51.6%. In fact, the RMSE average for Hitra was 6.16, which is higher than the previous two cases (Figure 9). This again further confirms that reproducibility of automated methods decreases as rock mass continuity decreases.

#### 4.1.4. Craignaw – Effect of Multi-Contrast Thresholds on Fracture Networks

For Craignaw, Ensemble I identified 11,276 features with an average length of 1.77 m, density of 0.192, and 2D intensity of 0.339. Ensemble II reduced features by 7.5% to 10,426, with an average length of 1.81 m, and density and 2D intensity of 0.163 and 0.296. Ensemble III detected 8,912 features, with an average length of 1.87 m, and density and 2D intensity of 0.139 and 0.261. Ensemble IV reduced features to 7,542, with an average length of 1.98 m, and density and 2D intensity of 0.118 and 0.233. Ensemble V saw a significant drop to 2,398 features, with an average length of 2.74 m, and density and 2D intensity decreasing to 0.037 and 0.103. Topology analysis

showed a reduction in nodes from 11,701 in Ensemble I to 3,142 in Ensemble V (Table 4).

Almost no features in Ensemble I had an average contrast above rock mass (0.3%), while 46.8% were between rock mass and vegetation contrast, and 51.9% below vegetation contrast (Figure 6G). In Ensemble V, no features were above rock mass contrast, 51.2% were between rock mass and vegetation contrast, and 48.8% below (Figure 5K). Major trends (NS, EW, NE/SW) persisted across all ensembles (Figure 6G, 6H).

The average feature contrast in Caignaw ranged from 82 in Ensemble I to 84 in Ensemble IV, with a slight decrease back to 82 in Ensemble V (Table 4). These fluctuations highlight the challenges posed by high vegetation percentage and low rock mass continuity, which is only 15.6%. The average feature contrast being close to the average vegetation contrast (81) rather than the rock mass contrast (163) indicates that the automated detection method often traces features in vegetated areas rather than in the rock mass. Lastly, for Caignaw, although fewer features were traced compared to previous cases, a much larger spread of length distributions can be observed (10.04) (Figure 8D). In fact, given the very low rock mass continuity in this case study, the larger spread between RMSE indicates higher variability and lower reproducibility in the fracture length measurements. The low continuity is contributing to the increased difficulty in consistently tracing features, leading to greater discrepancies in the length distributions across different ensembles. Following trends from previous case studies, this study confirms the hypothesis that rock mass continuity is the greatest contributing factor to reliable fracture tracing.

Location	Contrast Thresh. Max/min	# of fractures	Avg Length (m)	RMSE Ens. I/II Ens. I/III Ens. I/IV Ens. I/V Avg RMSE	# of nodes	Topology (%)	Density (F/m <sup>2</sup> )	2D Intensity ( $\Sigma$ Length/m <sup>2</sup> )
<b>Yosemite</b>								
<b>Ensemble I</b>	254/235	6,471	2.17	-	6,421	I:73; Y:23; X:4	0.103	0.217
<b>Ensemble II</b>	253/235	5,738	2.21	1.86	5,709	I:74; Y:23; X:3	0.091	0.202
<b>Ensemble III</b>	252/235	5,244	2.23	2.79	5,118	I:75; Y:23; X:2	0.083	0.185
<b>Ensemble IV</b>	251/235	4,826	2.25	2.29	4,858	I:75; Y:22; X:3	0.077	0.172
<b>Ensemble V</b>	250/230	2,395	2.49	6.18	2,702	I:80; Y:18; X:2	0.038	0.095
				3.56				
<b>Utah</b>								
<b>Ensemble I</b>	254/235	10,751	1.83	-	9,401	I:66; Y:30; X:4	0.173	0.281
<b>Ensemble II</b>	253/235	10,085	1.86	1.28	8,846	I:66; Y:30; X:4	0.162	0.268
<b>Ensemble III</b>	252/235	9,366	1.89	1.92	8,331	I:67; Y:29; X:4	0.151	0.254
<b>Ensemble IV</b>	251/235	8,912	1.91	2.07	8,088	I:68; Y:29; X:3	0.143	0.243
<b>Ensemble V</b>	250/230	4,440	2.24	11.10	4,733	I:75; Y:23; X:2	0.071	0.153
				5.20				
<b>Hitra</b>								
<b>Ensemble I</b>	254/235	14,652	1.47	-	12,836	I:66; Y:30; X:4	0.326	0.478
<b>Ensemble II</b>	253/235	13,440	1.50	1.28	11,964	I:67; Y:29; X:4	0.299	0.447
<b>Ensemble III</b>	252/235	12,353	1.54	2.42	11,263	I:69; Y:28; X:3	0.275	0.422
<b>Ensemble IV</b>	251/235	11,471	1.57	3.20	10,609	I:70; Y:27; X:3	0.255	0.400
<b>Ensemble V</b>	250/230	5,621	1.98	13.75	5,739	I:79; Y:20; X:1	0.125	0.232
				6.16				
<b>Craignaw</b>								
<b>Ensemble I</b>	254/235	12,276	1.77	-	11,701	I:71; Y:25; X:4	0.192	0.339
<b>Ensemble II</b>	253/235	10,426	1.81	2.15	10,055	I:73; Y:25; X:2	0.163	0.296
<b>Ensemble III</b>	252/235	8,912	1.87	2.98	8,825	I:75; Y:24; X:1	0.139	0.261
<b>Ensemble IV</b>	251/235	7,542	1.98	5.51	7,792	I:76; Y:21; X:3	0.118	0.233
<b>Ensemble V</b>	250/230	2,398	2.74	22.48	3,142	I:86; Y:13; X:1	0.037	0.103
				10.04				

Table 4: Properties of networks extracted automatically with the shearlet method

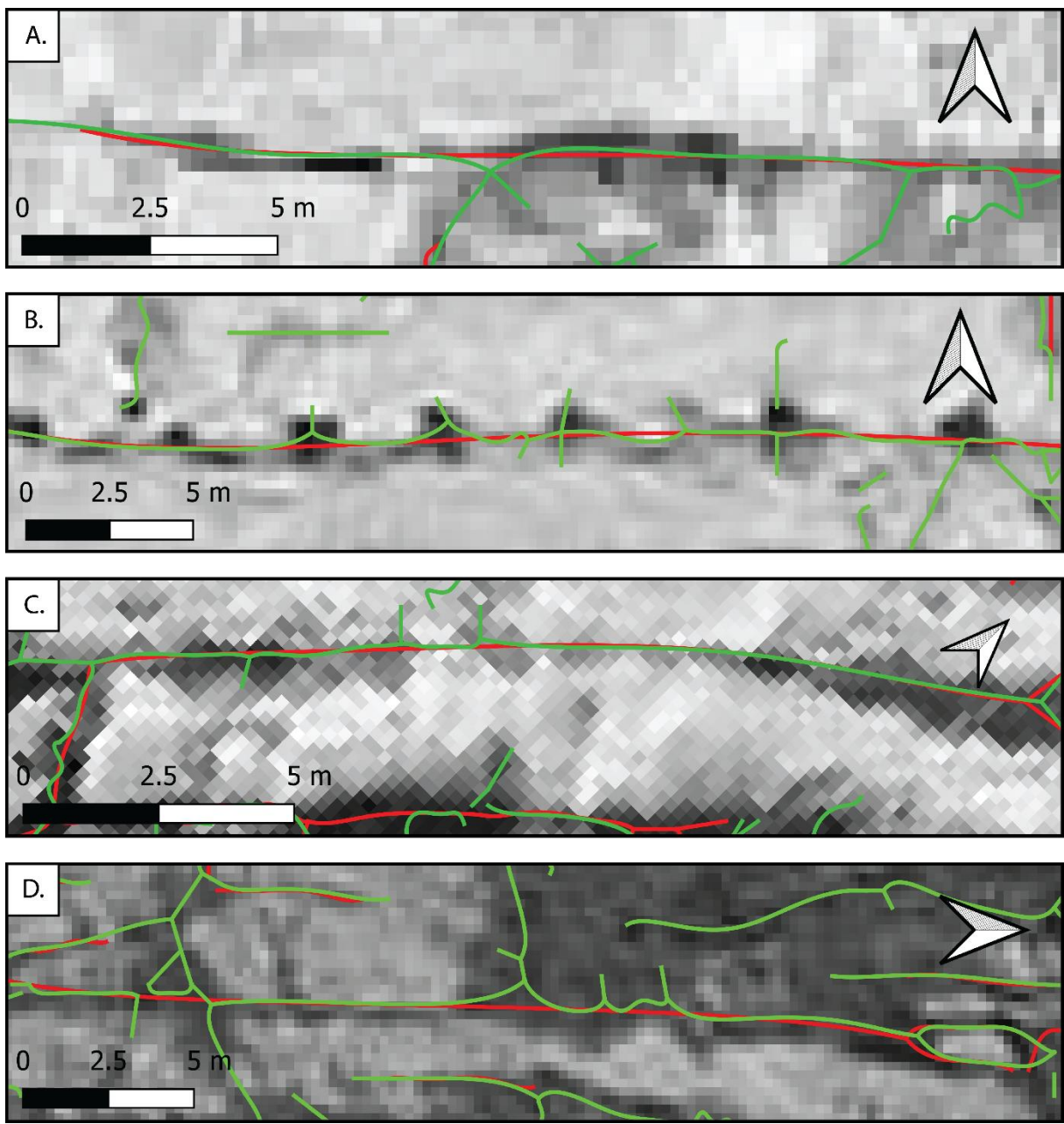


Figure 5: Comparison of features interpreted in Ensemble I (green) versus Ensemble V (red) for the four areas of interest: (A) Yosemite, (B) Utah, (C) Hitra, and (D) Craignaw. In all cases, Ensemble V produces more continuous features compared to Ensemble I, highlighting that higher contrast thresholds lead to a simplified fracture network by excluding lower-contrast segments.

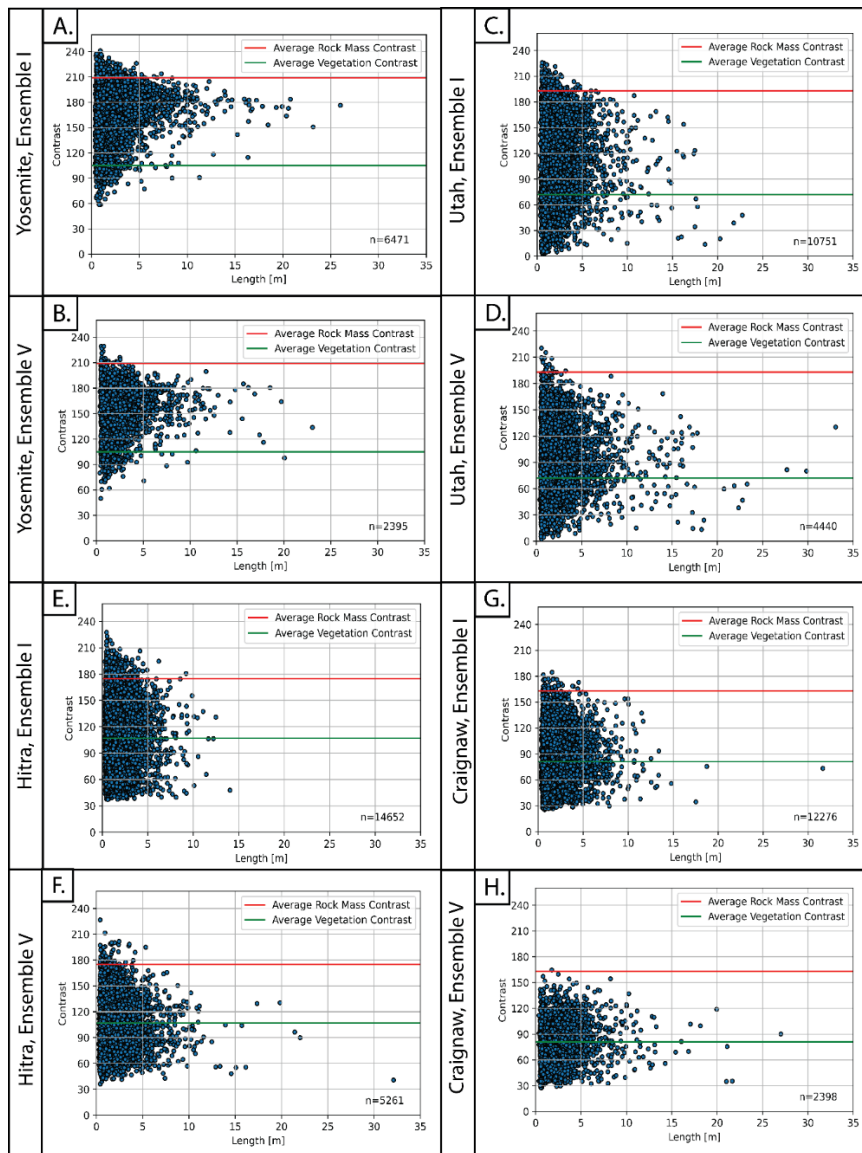


Figure 6: Relationship between fracture length and image contrast across Ensembles I and V for each study area: Yosemite (A–B), Utah (C–D), Hitra (E–F), and Craginaw (G–H). Horizontal lines indicate the average rock mass contrast (red) and average vegetation contrast (green) used as reference thresholds. Ensemble I (A, C, E, G) contains significantly more fractures than Ensemble V (B, D, F, H), demonstrating how increased thresholding reduces feature detection. Ensemble Vs tend to have a greater number of long features. Yosemite (A–B) and Utah (C–D) plots show higher overall contrasts and fewer low-contrast features. Hitra (E–F) and Craginaw (G–H) show the increasing influence of vegetation, with feature contrasts shifting towards darker (lower) values as vegetation coverage increases.

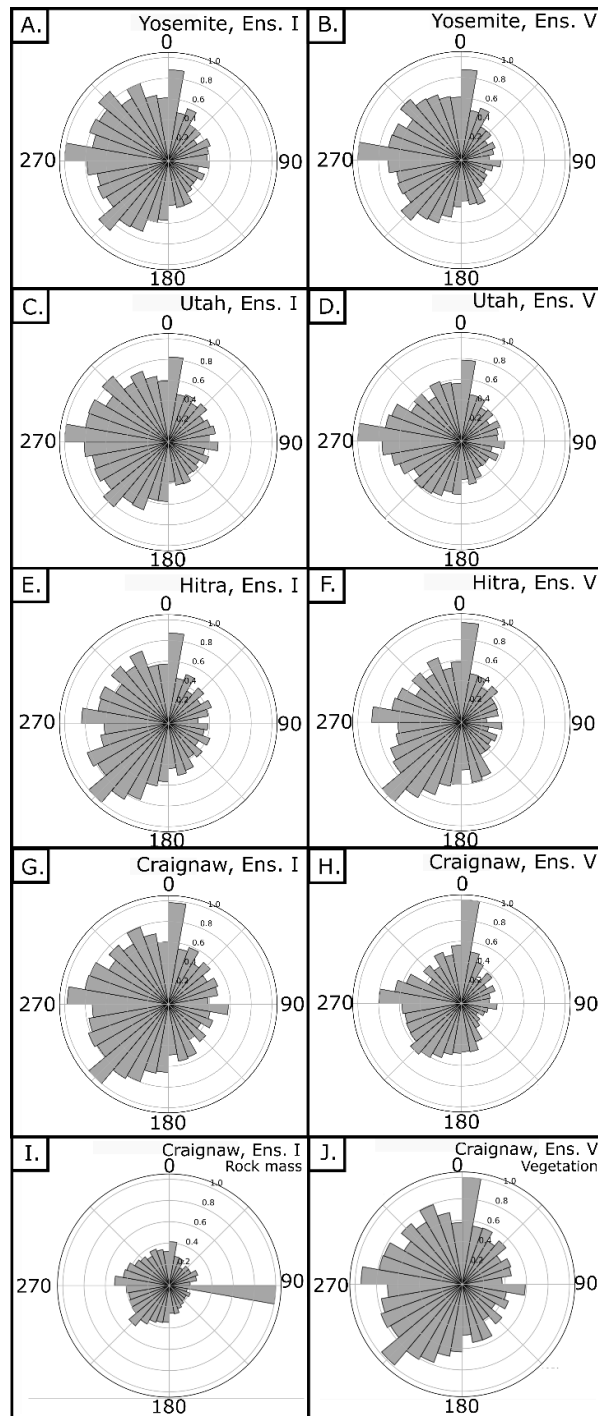
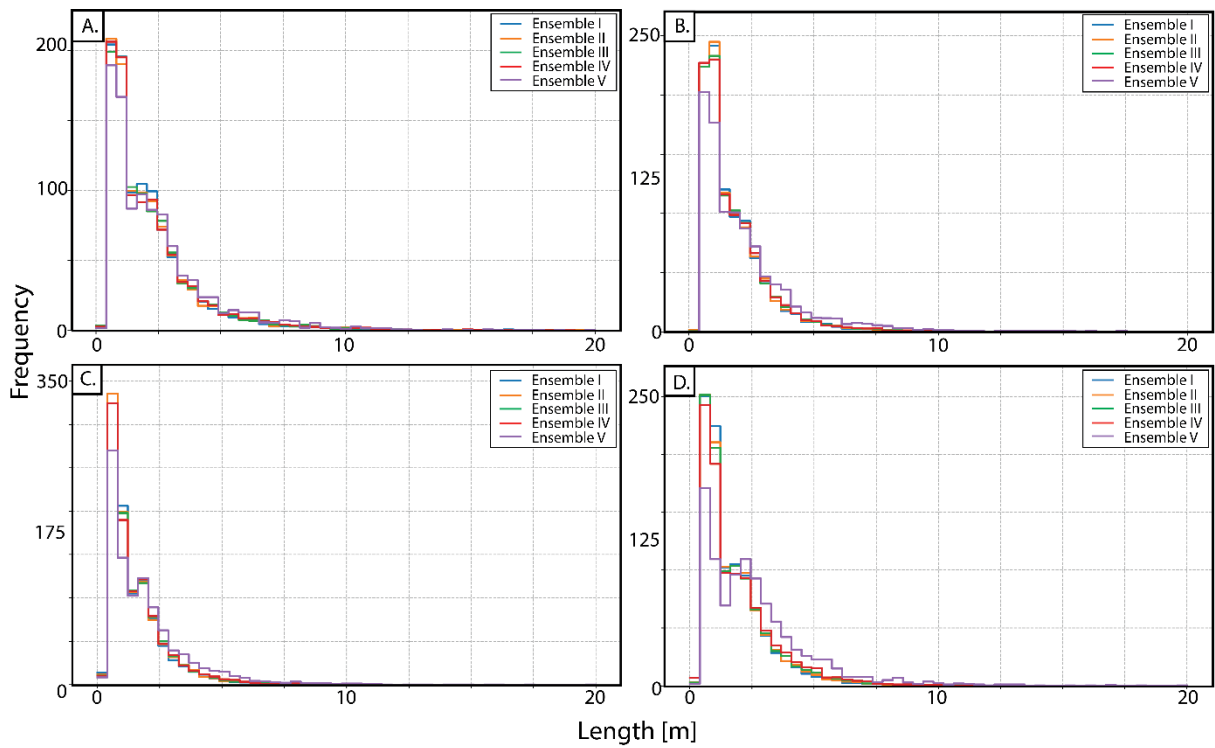


Figure 7: Diagrams A, C, E, and G are rose diagrams for Ensemble I in Yosemite, Utah, Hitra, and Craignaw, respectively, while B, D, F, and H represent Ensemble V for the same locations. Main orientations are consistent among all the ensembles. Plots I and J however show that there is a significant difference between figures traced solely in vegetation and features traced solely in rock mass.



*Figure 8: Length distribution plots for Yosemite (A), Utah (B), Hitra (C), and Cragshaw (D). Each line represents an ensemble, highlighting how variations in contrast thresholds impacts fracture length continuity. Yosemite (A) and Utah (B) show minimal variation between ensembles, which indicate higher reliability, whereas Hitra (C) and Cragshaw (D) display larger variations between ensembles, reflecting decreased reliability due to increased vegetation cover and lower rock mass continuity.*

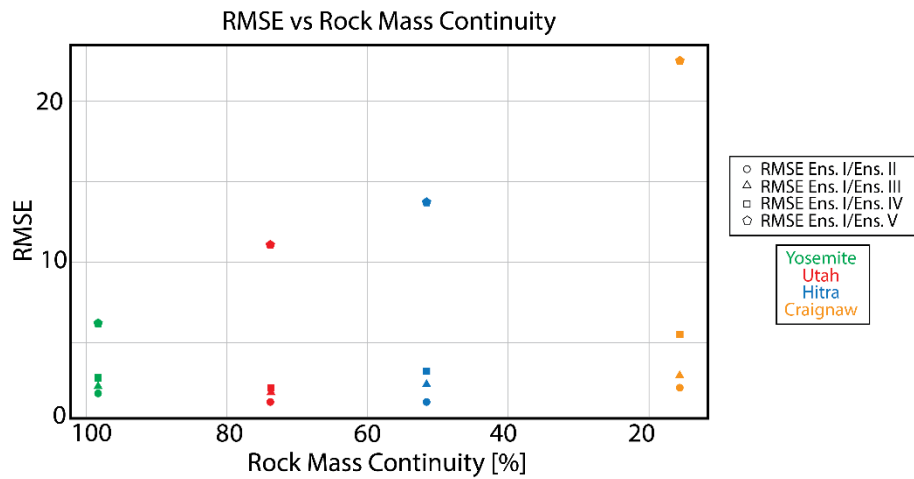


Figure 9: The Root Mean Square Error plotted against rock mass continuity and was calculated to visualize the effect of rock mass continuity on the reliability of automatically extracted networks, measured using RMSE.

#### 4.2. Characteristics of Extracted Networks – Binarization Method

Figure 10 presents the results for the Binarization method and Iterations A to D. Using the Binarization Method often results in numerous non-geological interpretations and circular artifacts (Figure 10), indicating the overall unreliability of the method. As the thresholds are lowered in the Binarization Method, results become increasingly comparable to those of the Shearlet Method.

However, the Binarization Method still struggles to maintain feature continuity at higher contrast thresholds, which often results in broken features that should be continuous for accurate geological interpretation.

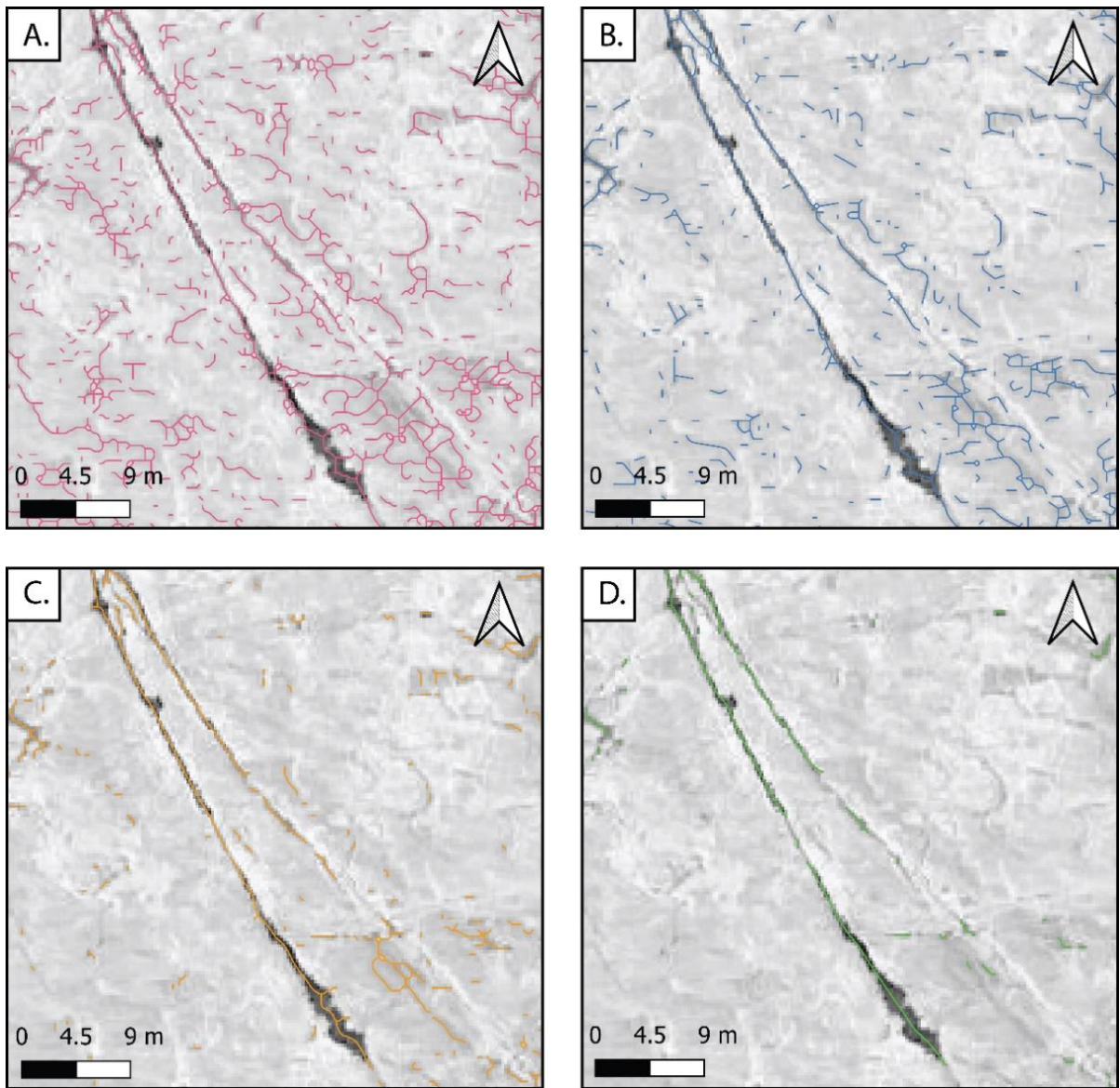


Figure 10: Results from four binarization iterations for Yosemite. (A) Threshold 210, (B) 205, (C) 195, (D) 175. (A) and (B) show many non-geological features and circular artifacts, while (C) and (D) display more geologically plausible results, highlighting the method's sensitivity to contrast thresholds.

#### 4.2.1. Yosemite – Effect of Single-Contrast Threshold on Fracture Networks

The results of the binarization method are summarized in Table 5. In Iteration A, 45,460 features were extracted with an average length of 2.07 m, a density of 0.70, and a 2D intensity of 0.67. Feature count decreased by 33.1% in Iteration B to 30,851,

with density and 2D intensity dropping to 0.49 and 0.48, respectively. Iteration C recorded 18,840 features, with density and 2D intensity further reduced to 0.29 and 0.32. Iteration D traced 8,319 features, with density at 0.13 and 2D intensity at 0.14 (Table 5).

Analysis of feature contrast (Figure 11A to D) shows that in Iteration A (210), 19.34% of features were above the average rock mass contrast of 209, 79.98% were between 209 and 105, and 0.51% were below 105. Iteration B (205) had 0.58% above 209, 97.84% between 105 and 209, and 1.53% below 105. In Iteration C (195) 6.01% of features were above 209, 92.72% between 209 and 105, and 1.07% below 105. Iteration D (175) had no features above 209, with 94.6% between 209 and 105, and 5.29% below 105. The lower threshold of 105 corresponds to the average contrast of vegetation in the dataset (Table 1); features below this value are likely unreliable due to potential confusion with vegetation or background noise. Fewer features were identified as contrast thresholds increased (Table 5).

The topology analysis (Table 5) reveal that in Iteration A, the network comprised 42,337 nodes with 43% I nodes, 55% Y nodes, and 2% X nodes. The node count decreased to 32,418 in Iteration B, with 55% I nodes, 44% Y nodes, and 1% X nodes. Iteration C had 23,065 nodes with 69% I nodes and 31% Y nodes. Iteration D had 12,720 nodes with 85% I nodes and 15% Y nodes.

The NS and EW orientations dominated across all iterations (Figure 12A to D), with consistent patterns suggesting potential extraction artifacts. The results show that increasing contrast thresholds (from Iteration A to D) significantly reduces the number of detected features and alters their properties. Higher thresholds filter out lower-intensity pixels, representing smaller or less distinct features, leading to a more fragmented and simplified network. This is evidenced by the decrease in feature count, density, and 2D intensity, and the shift in node proportions.

The comparison of average feature contrast supports these observations. As contrast thresholds increase from Iteration A to D, the average feature contrast decreases from 194 to 151. As we move to Iteration D, the Binarization Method, similarly to the Shearlet Method, is increasingly restricted to using darker pixels (low intensity). This means that fewer short, high-contrast features, which are often noise and non-geological, are detected. Consequently, only the longer, linear features, which are more likely to be geological, remain (Table 5). As a result, there is a greater differentiation between the average feature contrast and the average rock mass contrast (209), as the software primarily uses dark pixels to trace features.

In terms of reliability, upon comparing results to the network extracted using the Shearlet method for Yosemite, the Binarization Method was found to be much more unreliable, with a calculated average RMSE of 40.22, which is even higher than the RMSE for Cragshaw. The RMSE between Ensemble I and Iteration A was 39.78. This was expected, as the ImageJ method is considered a more "out-of-the-box" approach and is not as specialized as the Shearlet Method. This underlines the significant impact of the chosen image processing technique on the reliability of fracture length measurements.

Iteration #	Contrast Threshold	AVG Feature Contrast	# of fractures	AVG length (m)	# of nodes	Topology (%)	Density (F/m <sup>2</sup> )	2D Intensity ( $\Sigma$ Length/m <sup>2</sup> )
<b>Iteration A</b>	210	194	45460	2.07	42337	I:43; Y:55; X:2	0.70	0.67
<b>Iteration B</b>	205	184	30851	1.93	32418	I:55; Y:44; X:1	0.49	0.48
<b>Iteration C</b>	195	183	18840	1/82	23065	I:69; Y:31; X:0	0.29	0.32
<b>Iteration D</b>	175	151	8319	1.46	12720	I:85; Y:15; X:0	0.13	0.14

*Table 5: Properties of networks extracted automatically with the binarization method.*

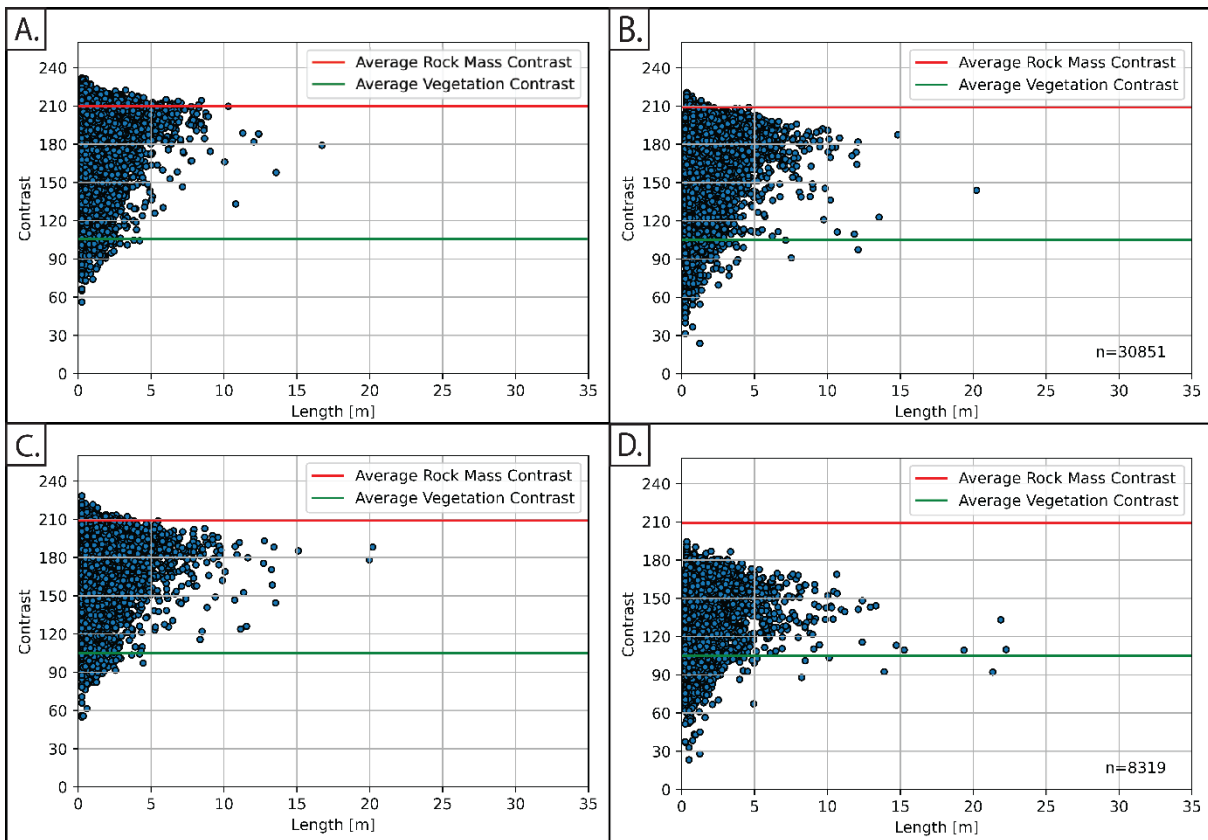


Figure 11: Scatter plots of length against average feature contrast. (A) contrast threshold 210; (B) contrast threshold 205; (C) contrast threshold 195; (D) contrast threshold 175. Red line is average rock mass contrast, at a value of 209; green line is average vegetation contrast, at a value of 105. Figures show the relative percentages of features above, between, and below vegetation and rock mass contrast for Iterations A (19.34%, 79.98%, 0.51%), B (0.58%, 97.84%, 1.53%), C (6.01%, 92.72%, 1.07%), and D (0%, 94.6%, 5.29%).

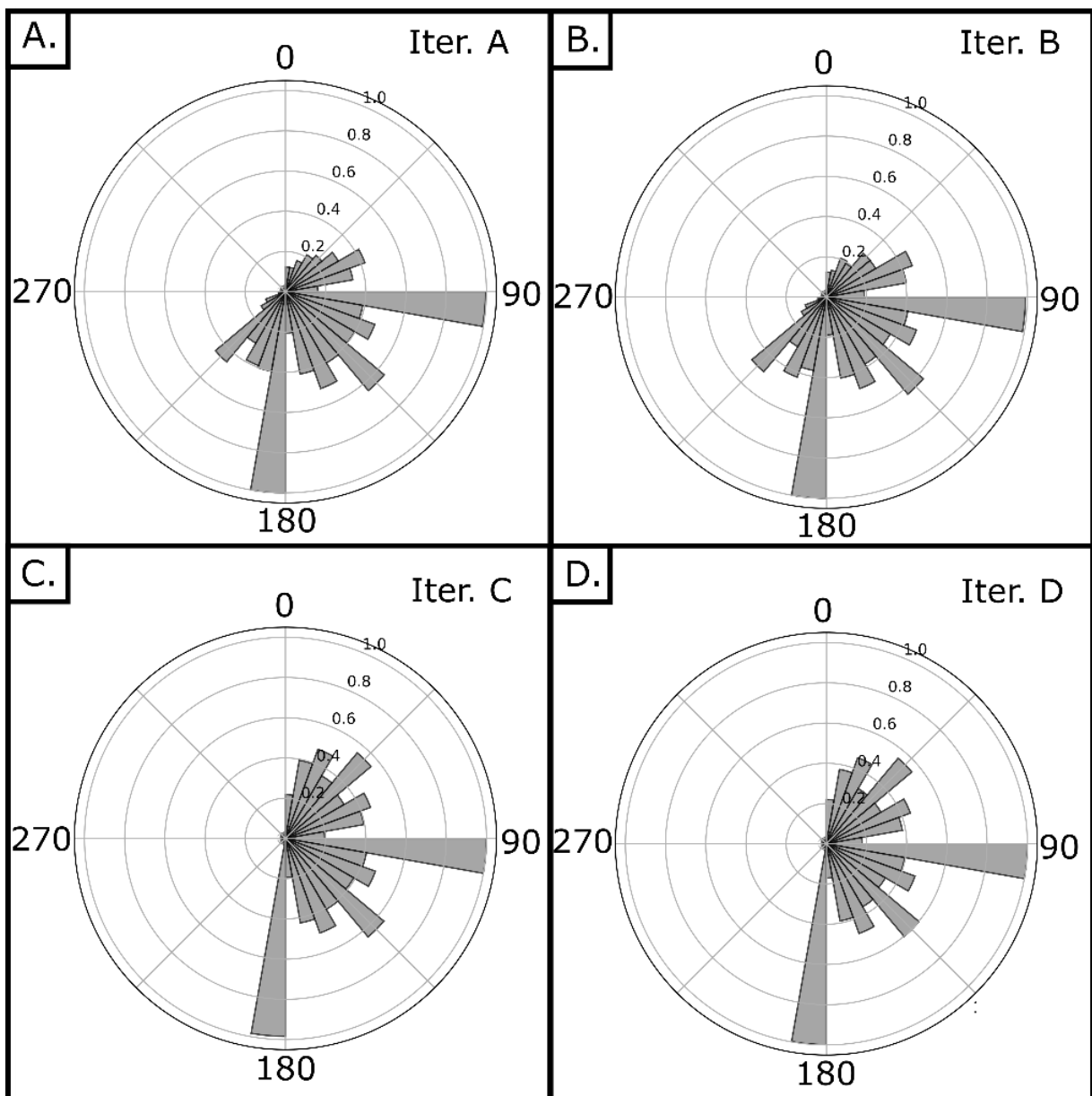


Figure 12: Rose diagrams of the lineaments extracted using the binarization method for four different iterations. (A) contrast threshold 210; (B) contrast threshold 205; (C) contrast threshold 195; (D) contrast threshold 175. The major difference amongst the four iterations is frequency. Orientations are all very similar across the four iterations.

#### 4.3. Network and Image Characteristics

Figure 13 shows cross plots how fracture network characteristics change because of using different contrast thresholds. Figure 13B is significant in that it

highlights the importance of understanding the exposure continuity when using automated approaches. Hitra and Cragshaw are the cases with the most fractures identified and are also the ones with the highest percentage of vegetation (48.8% and 84.4%, respectively). Because of the contrast similarity between fracture and vegetation, this has been translated to a very high foreground percentage, interpreted as features after skeletonization (Figure 13A, B). As the average feature contrast decreases, so does the total number of nodes (Figure 13D). This relationship occurs because lowering the contrast threshold causes the code to trace pixels with lower intensities (darker pixels), meaning the number of I nodes is increasing (Table 5). As the contrast threshold increases, the average feature contrast decreases, causing the code to increasingly restrict its tracing to darker pixels. In continuous exposures like Yosemite and Utah, we observe a positive correlation between the number of connections and average feature contrast. As contrast thresholds are progressively lowered from Iteration A to D, fewer features are extracted. Moreover, the average feature contrast decreases, indicating that as the threshold is lowered, the ImageJ method traces features in progressively darker areas. This results in the extraction of more, but generally shorter, features, as the algorithm becomes more sensitive to minor pixel intensity variations (Figure 13A). The study that narrow, high-contrast regions typically result in more robust feature extraction (Figure 13A).

There is a negative correlation between average feature contrast and the number of features identified using the binarization method (Figure 13A) and as the contrast threshold decreases, the number of features traced also decreases. This correlation is expected as the binarization method is increasingly restricted to darker pixels as the threshold is lowered, naturally resulting in fewer detectable features. In terms of reliability and reproducibility, this means that both methods' ability to consistently detect features is influenced by the contrast threshold setting, with lower

thresholds potentially compromising the reliability of feature detection by excluding high-intensity pixels, hence resulting in a more broken down network. A negative correlation between pixel connectedness and average feature length (Figure 13G) suggests that higher contrast thresholds may fragment longer features into shorter ones by excluding low-contrast pixels, whereas lower thresholds capture longer, more complete features but risk including non-meaningful ones.

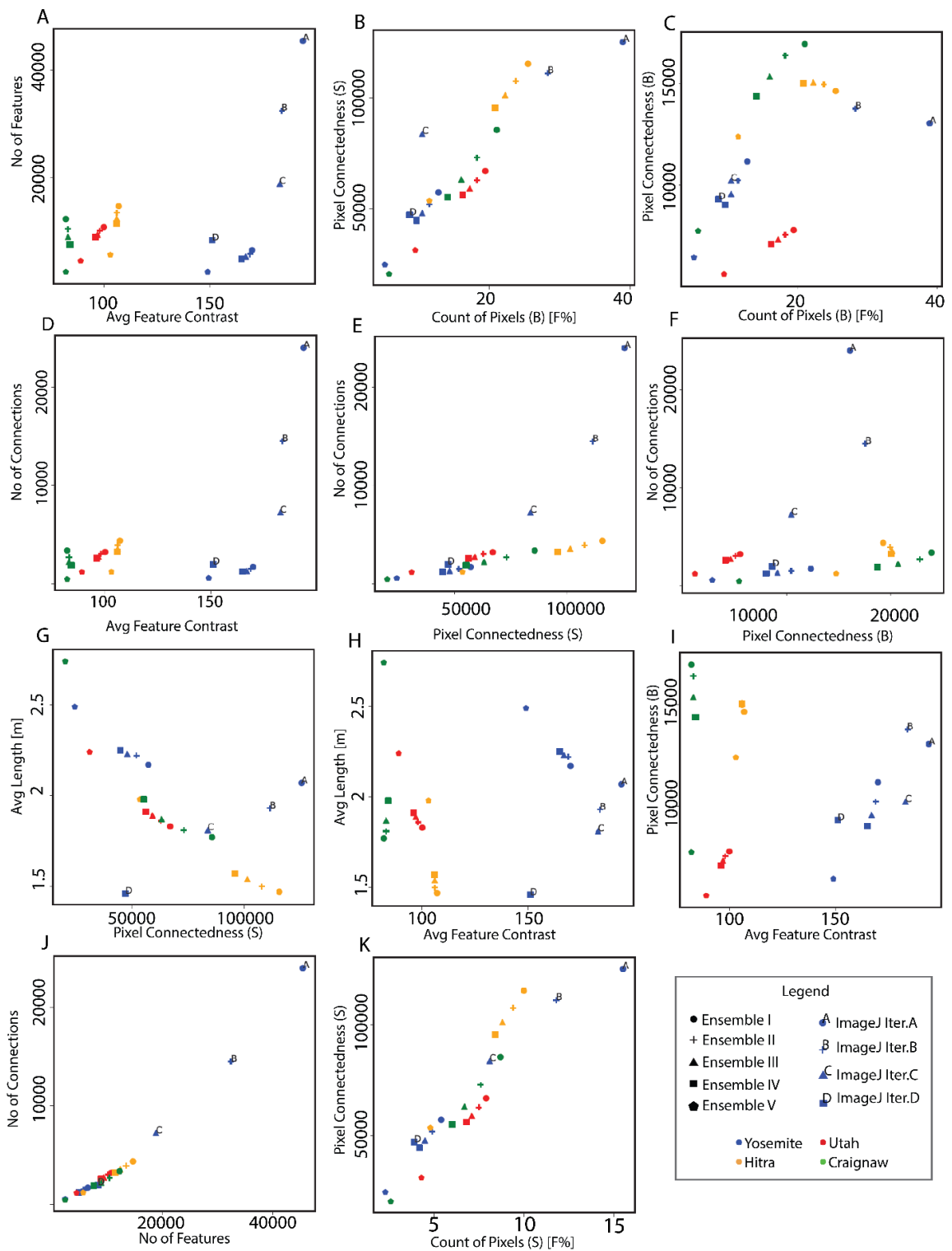


Figure 13: Cross plot analysis of lineament network characteristics influenced by varying contrasts. Plots reveal correlations between pixel connectivity, structural integrity, and contrast variations.

## 5. Discussion

The results presented demonstrate that fractures interpreted automatically from imagery are highly sensitive to the chosen contrast threshold value used, and that simplified single contrast thresholds are less reliable than the more complex methods, like the Shearlet Method, that take factor in the impact of varying the contrast value.

The results demonstrate that for outcrops with a high level of exposure continuity (e.g., Yosemite and Utah, Figure 1A, B), the two automated methods can produce reliable results (Figure 13B, C), as there is a lower chance of identifying features in vegetation. In low-continuity exposures like Hitra and Caignaw (Figure 1C, D), lowering the contrast threshold increases the likelihood of detecting features within darker areas of the imagery, which often correspond to vegetation in grayscale images (Figure 13). When the contrast between fractures and vegetation is subtle, the method's reliability decreases, as it becomes more difficult to distinguish true geological features from non-geological elements (Table 4).

### 5.1. Effects of contrast on fracture network properties

The variability in fracture network properties that result from varying the contrast threshold highlights the importance of analyzing the image contrast in automated feature extraction methods (Figure 13A, Table 4 and Table 5). Lower thresholds (Ensemble I) lead to more connections and shorter, fragmented features, while higher thresholds (Ensemble V) result in longer, more continuous features (Figure 5A, B, C, D), as also suggested by the negative correlation between pixel connectedness and average feature length (Figure 13G). In Ensemble I, lower contrast thresholds capture numerous short, interconnected features (green lines, Figure 13C,

F, I, L). As thresholds increase toward Ensemble V, networks shift toward fewer but longer and more continuous features (red lines), reflecting the focus on brighter, high-contrast areas. This trend is supported by a decrease in feature count and an increase in average feature length (Figure 13A).

Higher thresholds exclude darker pixels, reducing detectable features and increasing the percentage of I-Nodes, which signifies shorter features with fewer interactions, which signifies shorter features with fewer interactions (Table 5).

The impact of contrast thresholding is also evident across exposures with varying surface continuity. In Yosemite and Utah, where rock mass exposure is more continuous and vegetation is minimal, the imagery tends to have higher average feature contrast, which contributes to more reliable interpretations. In Hitra and Caignaw, both have a higher percentage of vegetation and lower rock mass continuity, leading to both methods repeatedly identifying features that are unlikely to be fractures.

Features detected in iterations A to D in the Binarization Method exhibit similar characteristics to those in the Shearlet Method. A lower contrast threshold results in fewer, fragmented features. The consistency of these effects across different methods indicates that careful consideration of contrast threshold is essential for accurate and reliable geological feature detection.

## 5.2. Effect of vegetation and exposure continuity

Vegetation and exposure continuity significantly affect the reliability of automated feature detection. Unreliable geological interpretations, such as the features inaccurately traced in shadows and vegetation (Figure 4E, F, G, H, Figure 11B, Table 4, Table 5), highlight the importance of considering the specific outcrop characteristics. In grayscale images, vegetation, shadows, and water bodies have similar contrast levels (60-150) to structural discontinuities, as shown Figure 4 and

Table 3. Both methods often detect features along the edges of such features. In regions with dense vegetation, automated methods, particularly at lower contrast thresholds, detect an increased number of features in both the vegetation and the rock mass. However, due to the similar grayscale values of vegetation and geological discontinuities, the methods are unable to reliably distinguish between the two. As a result, many of the additional features identified in vegetated areas are likely to be false positives, reducing the reliability of the detected networks. Upon visual inspection, many of these features do not appear to correspond to actual fractures (for instance, lines traced in/through vegetation or regions of the rock where no discernible fracture is visible), and are thus considered false positives (Figure 4). Although no formal ground-truth dataset is used for verification, these observations provide a practical check to distinguish real fractures from artifacts introduced by the automated process. The results show that two out of the three main identifiable trends (Figure 7I, J) may not be reliable, as they are solely traced in areas of vegetation and not in rock mass. Features traced solely on rock mass mainly trended EW (Figure 7I). In Ensemble I for Craginaw, the total number of traced features was 12,276, yet 9,854 features were traced on vegetation, accounting for approximately 78% of the total features, indicating suboptimal results. Therefore, the degree of pixel connectedness and the reliability of feature tracing are influenced by the contrast threshold levels, as higher pixel connectedness often correlates with more continuous and reliable features. Figure 13C shows that, in all Ensemble Vs for each case study, an increased contrast threshold corresponds to lower levels of pixel connectedness. This occurs because higher thresholds classify pixels with intensities above the threshold as background, causing the automated method to break up features and resulting in interrupted and fragmented features. Conversely, lower thresholds allow the method to trace darker features more continuously. After

analyzing the low RMSE values from Figure 88, 9 in relation to rock continuity parameters (Table 3), we observe that high RMSE values correspond with high rock mass exposure in Yosemite and Utah. This reinforces the reproducibility of automated feature detection in well-exposed geological settings. Conversely, Hitra and Cragshaw show lower rock continuity and higher RMSE values, indicating decreased reproducibility and highlighting the method's sensitivity to environmental conditions. Linear relationships between rock mass continuity and RMSE were hypothesized because the minimum contrast parameters were increased linearly during the analysis. This linear increase implies that features were traced using increasingly restricted portions of pixels with lower intensity (darker). As the contrast threshold rises, the set of detectable pixels changes predictably because each incremental change in the threshold systematically excludes the pixels with lower contrast. This systematic exclusion impacts the length of features, number of features, pixel connectedness, and other related metrics in a consistent and measurable manner. Our results supported this hypothesis. The conversion from binarized to skeletonized images in both methods is reproducible and reliable, indicated by the positive linear correlation between binarized and skeletonized pixel connectedness (Figure 13B, C). Figure 13E and Figure 13F show a linear correlation between the number of connections and pixel connectedness in both skeletonized and binarized images for both Shearlet method ensembles and Binarization method iterations. This indicates that an increase in pixel connectedness corresponds to more connections within the network, further confirming the reliability of the conversion from binarized images to skeletonized images.

The study reveals limitations in using decimeter resolution imagery with automatic methods for extracting features. The low RMSE in regions with substantial percentage of continuous rock exposure, such as Yosemite and Utah, indicate that

automated methods are more reproducible in these settings. However, this does not necessarily imply a reliable tracing of geological features. In areas with continuous exposures, the reduced presence of vegetation lowers the chance of tracing non-geological features, improving the method's effectiveness. Conversely, in settings like Cragshaw with minimal rock exposure, lower RMSE values point toward the potential misidentification of features due to the increased percentage of vegetation, which leads to the introduction of non-robust geological interpretation due to linear patterns being identified in vegetation. Moreover, the RMSE measured between Ensemble I using the Shearlet Method and Iteration A using the binarization method was 39.78, which provides a definitive measure of the unreliability of these automated approaches. This measure of RMSE serves as a critical indicator of the need for ongoing refinement and validation of automated techniques in geological analysis.

These findings underline that, while automated feature extraction can reduce interpretation time and improve reproducibility, their reliability on decimeter-resolution imagery heavily depends on exposure continuity. Decreased continuity directly impacts the network reliability extracted by automated methods, making the methods highly sensitive to image properties such as contrast levels and thresholds. Therefore, while automated methods work better with continuous exposure, the reliability of the features traced remains a primary concern.

### 5.3. Effects of lighting

The albedo of the rock mass, a measure of the amount of light reflected by a surface (e.g., Bemis et al., 2014), likely impacts the effectiveness of automated feature detection. High albedo can lead to overexposure in photographic or satellite imagery, obscuring detailed texture necessary for accurate feature identification, while low albedo can result in underexposure, diminishing contrast and making subtle features

difficult to detect (e.g., Maerz, Franklin, and Bennett 1990). Granitic rocks typically exhibit albedo ranging between 30% and 35% (Rees, 2013; Trimble, 1987), while dry desert sandstones have lower albedo values, ranging between 20% and 32% (Craft and Horel, 2019; Henderson-Sellers and Wilson, 1983). The high albedo of rock mass at Yosemite (Figure 3A) compared to Utah (Figure 3B) may reduce the contrast between features and rock mass. Fractures often appear as shadows due to the lack of incident light. If exposed, fracture surfaces would have a similar albedo to the rock mass. Additionally, clean fractures with no gap between edges can be obscured by the highly reflective rock surface. Features filled with material like the surrounding rock also have similar albedo, making detection challenging. Thus, high albedo can obscure both exposed fractures and tightly aligned breaks, reducing feature visibility. The combination of narrow feature apertures and high rock albedo can make contrast-based approaches more challenging, particularly in characterizing intersections due to the high reflectivity of the rock, which often masks narrow terminations.

The angle of light incidence with exposed rock when the image is acquired also plays a key role for the correct extraction of features (e.g., Jaud et al., 2019; Sekrecka, Wierzbicki, and Kedzierski, 2020; Walker and Trexler, 1977). For instance, as highlighted by the red box in Figure 4G, it is clear that the dark area is just a shadow of a cliff. Yet, when we look at the same picture in grayscale, the automatic methods mistook it for a geological feature because the shadow and the rock look similar in terms of lightness and darkness. Moreover, when the sun is low, it can cast shadows on the rocks, making them look like geological features to the automatic methods. Low light can also make real features hard to see and trace (Creus, Sanislav, and Dirks 2021).

#### 5.4. Challenges and Recommendations for Automated Lineament Detection Using Contrast-Based Methods

The findings of this study suggest that, while automated fracture detection methods relying on contrast differences in grayscale images to trace features are highly reproducible, they cannot always be considered reliable. In discontinuous exposures, automated methods confidently interpreting possible features through areas with vegetation cover can be challenging. The same challenge applies to the edges of outcrop exposures, which could be structural features. Automated methods accurately trace outcrop edges, but these may not represent geologically meaningful features and require careful validation. In contrast to image classification methods that use training data and machine learning (e.g., Harvey and Fotopoulos 2016; Reinhardt et al, 2022), contrast-based methods cannot incorporate prior geological information. Grayscale images have fewer unique values compared to three-band color images, potentially complicating accurate feature detection (Petrushan et al., 2023).

To optimize reliability and robustness of automated feature extraction it is recommended that:

- a) The sensitivity of feature networks to threshold parameters, such as contrast is evaluated and a rigorous quality control (QC) workflow post-extraction is established.
- b) Inaccurate interpretations can be mitigated by either a) conducting image pre-processing to exclude vegetation by assigning null values to vegetated areas, or implementing image post-processing, which requires selective feature removal based on defined criteria, involving user expertise.

## 6. Conclusions

The study reveals limitations in using decimeter resolution imagery with automatic methods for extracting features. The reliability and replicability of contrast-based methods are highly sensitive to image properties such as contrast levels and contrast thresholds. Additionally, outcrop characteristics like exposure continuity and vegetation percentage significantly impact the effectiveness of these methods. Exposure continuity in decimeter resolution aerial imagery also impacts feature detection reliability. While automated feature extraction methods reduce interpretation time, subjective biases, and improve reproducibility, their reliability on decimeter-resolution imagery depends widely on exposure continuity, as decreased continuity was observed to directly impact network reliability extracted by automated methods.

Understanding how contrast changes across an image, together with environmental factors like vegetation cover and exposure continuity, is crucial for accurate and reliable automated fracture detection. These findings can be extended to any automated contrast-based approach currently available, emphasizing that while automated methods can significantly aid geological investigations, their reliability is highly contingent upon appropriate parameter settings and image characteristics.

The workflow presented throughout this paper serves as a measure of the reliability of automated methods when applied to low-resolution imagery, and highlights their limitations and challenges. This study underscores the necessity of considering image properties and environmental conditions to ensure meaningful geological interpretations. By providing a detailed analysis of the impact of various parameters, this study offers valuable insights into optimizing automated fracture detection methods and improving their application in geological research.

## **Acknowledgements**

### **Author contributions**

**Gianluca Amicarelli (PhD Res.):** Writing – Original Draft, Project Administration, Data Curation, Conceptualization, Investigation, Validation, Methodology, Formal Analysis.

**Mark T. Ireland:** Writing – review and editing, Supervision, Conceptualization, Validation. **Colin T. Davie:** Writing – review and editing, Supervision, Conceptualization, Validation.

### **Data and code availability**

The MATLAB code for the Shearlet based method developed by Prabhakaran (2019) is available from: <https://doi.org/10.5194/se-10-2137-2019>

The input data for this work are available from <https://digimap.edina.ac.uk/>, <https://www.kartverket.no/>, <https://www.ogc.org/standard/wms/>

Dataset is available from <https://figshare.com/s/8f9f30edf4fcb22bbc9e>

ImageJ is available from <https://imagej.net/ij/download.html>

NetworkGT is available from: <https://github.com/BjornNyberg/NetworkGT>

## References

- Abu-Ain, Waleed, Siti Norul Huda Sheikh Abdullah, Bilal Bataineh, Tarik Abu-Ain, and Khairuddin Omar. 2013. "Skeletonization Algorithm for Binary Images." *4th International Conference on Electrical Engineering and Informatics, ICEEI 2013* 11:704–9. doi: 10.1016/j.protcy.2013.12.248.
- Alexandersen, Joe, and Casper Schousboe Andreasen. 2020. "A Review of Topology Optimisation for Fluid-Based Problems." *Fluids* 5(1):29. doi: 10.3390/fluids5010029.
- Alvarez, Leidy Laura, Leonardo José do Nascimento Guimarães, Igor Fernandes Gomes, Leila Beserra, Leonardo Cabral Pereira, Tiago Siqueira Miranda, Bruno Maciel, and José Antônio Barbosa. 2021. "Impact of Fracture Topology on the Fluid Flow Behavior of Naturally Fractured Reservoirs." *Energies* 14(17):5488.
- Andrews, Billy J., Jennifer J. Roberts, Zoe K. Shipton, Sabina Bigi, M. Chiara Tartarello, and Gareth Johnson. 2019. "How Do We See Fractures? Quantifying Subjective Bias in Fracture Data Collection." *Solid Earth* 10(2):487–516. doi: 10.5194/se-10-487-2019.
- Bateman, Paul C., and Jerry P. Eaton. 1967. "Sierra Nevada Batholith." *Science* 158(3807):1407–17. doi: 10.1126/science.158.3807.1407.
- Bear, J. 1993. "1 - Modeling Flow and Contaminant Transport in Fractured Rocks." Pp. 1–37 in *Flow and Contaminant Transport in Fractured Rock*, edited by Jacob Bear, C.-F. Tsang, and G. de Marsily. Oxford: Academic Press.
- Bemis, Sean P., Steven Micklethwaite, Darren Turner, Mike R. James, Sinan Akciz, Sam T. Thiele, and Hasnain Ali Bangash. 2014. "Ground-Based and UAV-Based Photogrammetry: A Multi-Scale, High-Resolution Mapping Tool for Structural Geology and Paleoseismology." *Journal of Structural Geology* 69:163–78. doi: 10.1016/j.jsg.2014.10.007.
- Berkowitz, Brian. 2002. "Characterizing Flow and Transport in Fractured Geological Media: A Review." *Advances in Water Resources* 25(8–12):861–84. doi: 10.1016/s0309-1708(02)00042-8.
- Bertrand, Lionel, Yves Géraud, and Marc Diraison. 2021. "Petrophysical Properties in Faulted Basement Rocks: Insights from Outcropping Analogues on the West

European Rift Shoulders." *Geothermics* 95:102144. doi: 10.1016/j.geothermics.2021.102144.

- Bøe, Reidulv, Mai Britt Mørk, David Roberts, and JORUNN VIGRAN. 2005. "Possible Mesozoic Sediments in Fault and Brecciation Zones in Frøyfjorden, Mid Norway." *Norges Geologiske Undersøkelse Bulletin* 443:29–35.
- Bond, Clare Elizabeth, Alan D. Gibbs, Zoe K. Shipton, and Serena Jones. 2007. "What Do You Think This Is?: 'Conceptual Uncertainty' In Geoscience Interpretation." *GSA Today* 17(11):4–10. doi: 10.1130/GSAT01711A.1.
- C. Saravanan. 2010. "Color Image to Grayscale Image Conversion." Pp. 196–99 in *2010 Second International Conference on Computer Engineering and Applications*. Vol. 2.
- Canny, J. 1986. "A Computational Approach to Edge Detection." *IEEE Transactions on Pattern Analysis and Machine Intelligence* PAMI-8(6):679–98. doi: 10.1109/TPAMI.1986.4767851.
- Castaing, C., M. A. Halawani, F. Gervais, J. P. Chilès, A. Genter, B. Bourguine, G. Ouillon, J. M. Brosse, P. Martin, A. Genna, and D. Janjou. 1996. "Scaling Relationships in Intraplate Fracture Systems Related to Red Sea Rifting." *Tectonophysics* 261(4):291–314. doi: 10.1016/0040-1951(95)00177-8.
- Chen, Jiayao, Mingliang Zhou, Hongwei Huang, Dongming Zhang, and Zhicheng Peng. 2021. "Automated Extraction and Evaluation of Fracture Trace Maps from Rock Tunnel Face Images via Deep Learning." *International Journal of Rock Mechanics and Mining Sciences* 142:104745. doi: <https://doi.org/10.1016/j.ijrmmms.2021.104745>.
- Cracknell, Matthew J., and Anya M. Reading. 2014. "Geological Mapping Using Remote Sensing Data: A Comparison of Five Machine Learning Algorithms, Their Response to Variations in the Spatial Distribution of Training Data and the Use of Explicit Spatial Information." *Computers & Geosciences* 63:22–33. doi: 10.1016/j.cageo.2013.10.008.
- Craft, Kevin M., and John D. Horel. 2019. "Variations in Surface Albedo Arising from Flooding and Desiccation Cycles on the Bonneville Salt Flats, Utah." *Journal of Applied Meteorology and Climatology* 58(4):773–85. doi: 10.1175/JAMC-D-18-0219.1.

- Creus, P. K., I. V. Sanislav, and P. H. G. M. Dirks. 2021. "Application of SfM-MVS for Mining Geology: Capture Set-up and Automated Processing Using the Dugald River Zn-Pb-Ag Mine as a Case Study." *Engineering Geology* 293:106314. doi: 10.1016/j.enggeo.2021.106314.
- Esri. 2023a. "Raster to Polyline (Conversion)." Retrieved (<https://pro.arcgis.com/en/pro-app/latest/tool-reference/conversion/raster-to-polyline.htm>).
- Esri. 2023b. "World Imagery." *ArcGis.Com*. Retrieved ([https://www.arcgis.com/home/item.html?id=10df2279f9684e4a9f6a7f08febac2a9%3FWT.mc\\_id%3DEmailCampaign15361](https://www.arcgis.com/home/item.html?id=10df2279f9684e4a9f6a7f08febac2a9%3FWT.mc_id%3DEmailCampaign15361)).
- Gabrielsen, Roy H., and Alvar Braathen. 2014. "Models of Fracture Lineaments — Joint Swarms, Fracture Corridors and Faults in Crystalline Rocks, and Their Genetic Relations." *Tectonophysics* 628:26–44. doi: 10.1016/j.tecto.2014.04.022.
- Gardiner, C. I., and S. H. Reynolds. 1932. "The Loch Doon 'Granite' Area, Galloway." *Quarterly Journal of the Geological Society* 88(1–4):1-NP. doi: 10.1144/gsl.jgs.1932.088.01-04.03.
- Gautneb, Havard, and David Roberts. 1989. "Geology and Petrochemistry of the Smola-Hitra Batholith, Central Norway." (416):1–24.
- Gilluly, James, and J. B. Reeside Jr. 1928. *Sedimentary Rocks of the San Rafael Swell and Some Adjacent Areas in Eastern Utah. Report*. 150D. doi: 10.3133/pp150D.
- Gudmundsson, Agust. 2011. *Rock Fractures in Geological Processes*. Cambridge University Press.
- Harvey, A. S., and G. Fotopoulos. 2016. "GEOLOGICAL MAPPING USING MACHINE LEARNING ALGORITHMS." *The International Archives of the Photogrammetry, Remote Sensing and Spatial Information Sciences* XLI-B8:423–30. doi: 10.5194/isprs-archives-XLI-B8-423-2016.
- Henderson-Sellers, A., and MF Wilson. 1983. "Surface Albedo Data for Climatic Modeling." *Reviews of Geophysics* 21(8):1743–78.
- Hines, Richard, Scott R. Paterson, Valbone Memeti, and Jennifer A. Chambers. 2018. "Nested Incremental Growth of Zoned Upper Crustal Plutons in the Southern Uplands Terrane, UK: Fractionating, Mixing, and Contaminated Magma Fingers." *Journal of Petrology* 59(3):483–516. doi: 10.1093/petrology/egy034.

- Howell, John A., Allard W. Martinius, and Timothy R. Good. 2014. "The Application of Outcrop Analogues in Geological Modelling: A Review, Present Status and Future Outlook." *Geological Society, London, Special Publications* 387(1):1–25.
- Hung, Lisa, Okke Batelaan, and F. Smedt. 2005. "Lineament Extraction and Analysis, Comparison of LANDSAT ETM and ASTER Imagery. Case Study: Suoimuoi Tropical Karst Catchment, Vietnam." *Proc SPIE* 5983. doi: 10.1117/12.627699.
- ImageJ. 2023. "Analyze Particles." Retrieved (<https://imagej.net/imaging/particle-analysis>).
- ImageJ. 2024. "AnalyzeSkeleton." Retrieved (<https://imagej.net/imagej-wiki-static/AnalyzeSkeleton>).
- Jaud, Marion, Pauline Letortu, Claire Théry, Philippe Grandjean, Stéphane Costa, Olivier Maquaire, Robert Davidson, and Nicolas Le Dantec. 2019. "UAV Survey of a Coastal Cliff Face – Selection of the Best Imaging Angle." *Measurement* 139:10–20. doi: 10.1016/j.measurement.2019.02.024.
- Kartverket. 2013. *Produktspesifikasjon for Ortofoto i Norge*. 3507 Hønefoss: Kartverket.
- Kozłowska, Polina, Adrianna Łobodzińska, Klaudia Lewita, and Tymoteusz Miller. 2023. *APPLYING MACHINE LEARNING TO IMAGE RECOGNITION TECHNIQUES FOR ENHANCED GEOLOGICAL ANALYSIS AND SOCIETAL IMPACT*.
- Kutyniok, Gitta, and Demetrio Labate. 2012. "Introduction to Shearlets." Pp. 1–38 in *Shearlets: Multiscale Analysis for Multivariate Data*.
- Labate, D.; Lim. 2005. "Sparse Multidimensional Representation Using Shearlets." *Wavelets Optics and Photonics XI*.
- Maerz, N. H., J. A. Franklin, and C. P. Bennett. 1990. "Joint Roughness Measurement Using Shadow Profilometry." *International Journal of Rock Mechanics and Mining Sciences & Geomechanics Abstracts* 27(5):329–43. doi: 10.1016/0148-9062(90)92708-M.
- MathWorks. 2023a. "Depth First Search (DFS) Algorithm." Retrieved (<https://www.mathworks.com/help/matlab/ref/graph.dfsearch.html>).
- MathWorks. 2023b. "Rgb2gray."
- Miranda, M. M., N. Giordano, J. Raymond, A. J. S. C. Pereira, and C. Dezayes. 2020. "Thermophysical Properties of Surficial Rocks: A Tool to Characterize

Geothermal Resources of Remote Northern Regions." *Geothermal Energy* 8(1). doi: 10.1186/s40517-020-0159-y.

Newell Andrew J. and Shariatipour Seyed M. 2016. "Linking Outcrop Analogue with Flow Simulation to Reduce Uncertainty in Sub-Surface Carbon Capture and Storage: An Example from the Sherwood Sandstone Group of the Wessex Basin, UK." *Geological Society, London, Special Publications* 436(1):231–46. doi: 10.1144/SP436.2.

Nhat-Duc, Hoang, Quoc-Lam Nguyen, and Van-Duc Tran. 2018. "Automatic Recognition of Asphalt Pavement Cracks Using Metaheuristic Optimized Edge Detection Algorithms and Convolution Neural Network." *Automation in Construction* 94:203–13. doi: 10.1016/j.autcon.2018.07.008.

Njue, Lucy Muthoni. 2010. "Geological Field Mapping." *A Paper Presented at Short Course V on Exploration for Geothermal Resources, Organized by United Nations University-Geothermal Training Programme, Geothermal Development Company and KenGen, at Lake Bogoria and Lake Naivasha, Kenya.*

Nyberg, Björn, Casey W. Nixon, and David J. Sanderson. 2018. "NetworkGT: A GIS Tool for Geometric and Topological Analysis of Two-Dimensional Fracture Networks." *Geosphere* 14(4):1618–34. doi: 10.1130/ges01595.1.

Petrushan, M., Yu Vermenko, D. Shaposhnikov, and S. Anishchenko. 2013. "Comparative Analysis of Color-and Grayscale-Based Feature Descriptions for Image Recognition." *Pattern Recognition and Image Analysis* 23:415–18.

Prabhakaran, Rahul, Pierre-Olivier Bruna, Giovanni Bertotti, and David Smeulders. 2019. "An Automated Fracture Trace Detection Technique Using the Complex Shearlet Transform." *Solid Earth* 10(6):2137–66. doi: 10.5194/se-10-2137-2019.

Prabhakaran, Rahul, J. L. Urai, G. Bertotti, C. Weismüller, and D. M. J. Smeulders. 2021. "Large-Scale Natural Fracture Network Patterns: Insights from Automated Mapping in the Lilstock (Bristol Channel) Limestone Outcrops." *Journal of Structural Geology* 150:104405. doi: 10.1016/j.jsg.2021.104405.

Pruess, KARSTEN, and TN Narasimhan. 1982. "On Fluid Reserves and the Production of Superheated Steam from Fractured, Vapor-Dominated Geothermal Reservoirs." *Journal of Geophysical Research: Solid Earth* 87(B11):9329–39.

- Rakesh, Gupta, and Kaur Rajpreet. 2008. "Skeletonization Algorithm for Numeral Patterns." *International Journal of Signal Processing, Image Processing and Pattern Recognition* 1(1):63–72.
- Ray, Richard Godfrey. 1960. *Aerial Photographs in Geologic Interpretation and Mapping*. US Government Printing Office.
- Rees, William Gareth. 2013. *Physical Principles of Remote Sensing*. Cambridge university press.
- Reinhardt, Marcel, Arne Jacob, Saeid Sadeghnejad, Francesco Cappuccio, Pit Arnold, Sascha Frank, Frieder Enzmann, and Michael Kersten. 2022. "Benchmarking Conventional and Machine Learning Segmentation Techniques for Digital Rock Physics Analysis of Fractured Rocks." *Environmental Earth Sciences* 81(3):71.
- Rueden, Curtis T., Johannes Schindelin, Mark C. Hiner, Barry E. DeZonia, Alison E. Walter, Ellen T. Arena, and Kevin W. Eliceiri. 2017. "ImageJ2: ImageJ for the next Generation of Scientific Image Data." *BMC Bioinformatics* 18:1–26.
- Saibi, Hakim, Mohand Bersi, Mohamed Bodruddoza Mia, Nureddin Mohamed Saadi, Khalid Mohamed Saleh Al Bloushi, and Robert W. Avakian. 2018. "Applications of Remote Sensing in Geoscience." in *Recent Advances and Applications in Remote Sensing*. InTech.
- Sanderson, David J., and Casey W. Nixon. 2018. "Topology, Connectivity and Percolation in Fracture Networks." *Journal of Structural Geology* 115:167–77. doi: 10.1016/j.jsg.2018.07.011.
- Santos, Cristiana, and Lucien Rapp. 2019. "Satellite Imagery, Very High-Resolution and Processing-Intensive Image Analysis: Potential Risks Under the GDPR." *Air and Space Law* 44. doi: 10.54648/AILA2019018.
- Sarp, Gülcan. 2005. "Lineament Analysis from Satellite Images, North-West of Ankara." Masters Thesis, Middle East Technical University.
- Sekrecka, Aleksandra, Damian Wierzbicki, and Michal Kedzierski. 2020. "Influence of the Sun Position and Platform Orientation on the Quality of Imagery Obtained from Unmanned Aerial Vehicles." *Remote Sensing* 12(6). doi: 10.3390/rs12061040.
- Singhal, B. B. S., and R. P. Gupta. 2010. *Applied Hydrogeology of Fractured Rocks: Second Edition*. Springer Science & Business Media.

- Soller, David R., Taryn A. Lindquist, and Jonathan C. Matti. 2002. "Field Description of the Scientific and Locational Accuracy of Geologic Features (a Part of the Draft FGDC Geologic Map Symbolization Standard)." P. 33 in Vol. 2. Citeseer.
- Tartaglia, Giulia, Alberto Ceccato, Thomas Scheiber, Roelant van der Lelij, Jasmin Schönenberger, and Giulio Viola. 2022. "Time-Constrained Multiphase Brittle Tectonic Evolution of the Onshore Mid-Norwegian Passive Margin." *GSA Bulletin* 135(3-4):621-42. doi: 10.1130/B36312.1.
- Taylor, John R., and Sarah Taylor Lovell. 2012. "Mapping Public and Private Spaces of Urban Agriculture in Chicago through the Analysis of High-Resolution Aerial Images in Google Earth." *Landscape and Urban Planning* 108(1):57-70. doi: 10.1016/j.landurbplan.2012.08.001.
- Thiele, S. T., L. Grose, A. Samsu, S. Micklethwaite, S. A. Vollgger, and A. R. Cruden. 2017. "Rapid, Semi-Automatic Fracture and Contact Mapping for Point Clouds, Images and Geophysical Data." *Solid Earth* 8(6):1241-53. doi: 10.5194/se-8-1241-2017.
- Tindle, Andrew G., and Julian A. Pearce. 1981. "Petrogenetic Modelling of in Situ Fractional Crystallization in the Zoned Loch Doon Pluton, Scotland." *Contributions to Mineralogy and Petrology* 78(2):196-207. doi: 10.1007/BF00373781.
- Trimble, V. 1987. "Crc Handbook of Chemistry and Physics-Weast, Rc." *Scientist* 1(25):19-19.
- UGRC. 2023. "High Resolution Orthophotography." *Utah Geospatial Resource Center*. Retrieved (<https://gis.utah.gov/data/aerial-photography/hro/#HRO2009>).
- Voorn, Maarten, Ulrike Exner, and Alexander Rath. 2013. "Multiscale Hessian Fracture Filtering for the Enhancement and Segmentation of Narrow Fractures in 3D Image Data." *Computers & Geosciences* 57:44-53. doi: 10.1016/j.cageo.2013.03.006.
- Walker, Patrick M., and Dennis T. Trexler. 1977. "Low Sun-Angle Photography." *Photogrammetric Engineering and Remote Sensing* 43(4):493.
- Weismüller, C., R. Prabhakaran, M. Passchier, J. L. Urai, G. Bertotti, and K. Reicherter. 2020. "Mapping the Fracture Network in the Lilstock Pavement, Bristol Channel, UK: Manual versus Automatic." *Solid Earth* 11(5):1773-1802. doi: 10.5194/se-11-1773-2020.

Wilson, C. E. Bond, and T. F. Shipley. 2019. "How Can Geologic Decision-Making under Uncertainty Be Improved?" *Solid Earth* 10(5):1469–88. doi: 10.5194/se-10-1469-2019.

Witherspoon, PA, NGW Cook, and JE Gale. 1980. *GEOLOGIC STORAGE OF RADIOACTIVE WASTE: RESULTS OF FIELD INVESTIGATIONS AT STRIPA, SWEDEN*. techreport.